Research Report

Non-linear wave loads on next-generation offshore wind turbines

Offshore and Dredging Engineering
Tim Holsappel

Delft University of Technology

TU Delft

Research Report

Non-linear wave loads on next-generation offshore wind turbines

by

Tim Holsappel

Student Name	Student Number
Tim Holsappel	4496132

TU supervisor:	Dr. G. Lavidas
SGRE supervisors:	Dr. D.P. Rijnsdorp & Ir. M. van der Meulen
Project Duration:	February 2023 - December 2023
Faculty:	Faculty of Mechanical, Maritime and Materials Engineering, Delft

Cover:	SG 14-222 DD by Siemens Gamesa Renewable Energy
Style:	TU Delft Report Style

TU Delft

Contents

1

Introduction

In recent decades, the size of wind turbines and their support structures has experienced exponential growth in response to the ever-increasing demand for renewable energy. This expansion is primarily driven by the growing demand and the market's competitive nature, where larger turbines offer greater efficiency (Amano, 2017). However, this increase in size poses significant challenges, particularly when wind turbines are subjected to large waves during severe storms. The natural frequency of wind turbines and their structures decreases as their size increases. This leads to potential resonance-related issues when their eigenfrequency overlaps with the frequencies of these large waves, resulting in increased accelerations and loads (Velarde et al., 2019).

To ensure a safe and cost-effective design, it is necessary to accurately model these waves, as their loads are increasingly found to be driving the design (Schløer et al., 2016). The problem with modelling these waves emerging from severe storms is that their shapes are mainly asymmetrical (non-linear), and their kinematics are thus not captured well by the linear wave theory. The current approach to calculating wave loads on wind turbines relies on embedding higher-order non-linear waves, generated by the stream function, into linear theory (Suja-Thauvin et al., 2018). This methodology has been widely used due to its simplicity and computational efficiency. However, recent studies have highlighted uncertainties associated with this approach when applied to large steep non-linear waves (Peeringa, 2004). Where post-breaking and breaking waves result in underestimated wave loads.

Wave breaking is one of the driving factors in the need for a better non-linear wave modelling method. Wave breaking occurs when the steepness of a wave exceeds a certain threshold, causing the wave's crest to collapse. The most well-known breaking wave type is the plunging breaking wave, which can be seen in Figure 1.1. Wave breaking contributes to the highest ultimate loads and can not be captured with linear theory (Tang et al., 2020). Furthermore, the current approach is not able to simulate these breaking waves.

Figure 1.1: National Environmental Satellite, Data, and Information Service. (2013). Plunging breaking wave. Retrieved from http://www.nesdis.noaa.gov/news_archives/wod_2013.html

Recognising the uncertainty in the current calculation method, there is a pressing need to implement new techniques for simulating non-linear waves and accurately predicting wave loads on wind turbines. One of these ways is to use computational fluid dynamics (CFD), but due to the large number of calculations involved in the design process, CFD models are not viable due to the high computational costs. As an alternative, several recent studies have shown that modelling fully non-linear numerical wave models (NWMs) as numerical wave tanks (NWTs) can provide wave loads on offshore wind turbines; these models require less computational expense, are less accurate but do account for the non-linear effects seen with post-breaking and breaking waves that result in asymmetric wave shapes (Bredmose et al., 2016; Wang et al., 2021). NWTs have two methods to calculate the forces on a structure, either by using the Morison equation or by putting a structure in the wave tank and measuring the pressure. The latter can only be done in three-dimensional (3D) simulations as the waves need to pass around the structure, 3D simulations are too computationally expensive, and due to this reason, the Morison equation will be used so that the NWT can be set to two dimensional (2D). An overview of the different forcing methods per solution can be found in Figure 1.2

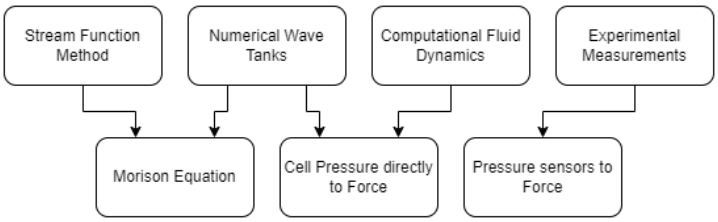

Figure 1.2: Different methods to calculate the forces exerted on a structure

The issues mentioned have led to the following research question;

What insights can be gained from numerical wave models in analysing the impact of non-linear waves on next-generation wind turbines?

The research question is divided into three subquestions, each focusing on a specific aspect of the numerical wave models used in this paper, OceanWave3D and SWASH. The first question aims to compare the capabilities of these NWTs, particularly in linear- and non-linear conditions, but also in speed, resolution, and accuracy across different depths and conditions. Various tests will be conducted to achieve this, and the results will be analysed and compared. The second question will focus on setting the tuneable breaking criterion in OW3D to make sure that the output aligns as much with SWASH as possible. This has led to the following research questions;

1. How do the numerical wave tanks modelled in OceanWave3D and SWASH compare their capabilities in simulating linear and non-linear wave behaviour across different depths and conditions, considering factors such as speed, resolution, and accuracy?
2. What is the optimal setting for the breaking criterion of OW3D to make sure it aligns with the response seen in SWASH?

The third question will focus on applying SWASH and OW3D in non-linear mode to numerical short-term storm sea states on a next-generation wind turbine. After this is done, a study into the load on these wind turbines will be performed. The outcome will be compared to the conventional industry-used stream function method. The Morison equation will be used for load calculations. This leads to the third and final research question;

3. How does applying SWASH and/or OW3D in non-linear mode, considering both regular- and steep short-term sea state wave load cases, affect the response of next-generation wind turbines compared to utilizing the industry-used stream function method?

Overall, this research project seeks to provide valuable insights into the capabilities of OceanWave3D and SWASH and their applicability in aiding in simulating the behaviour of wind turbines under different load conditions. What is of particular importance is to see how the increased accuracy of

these models can provide a better picture of the increasing loads on next-generation wind turbines. The results obtained from this research will be beneficial for deepening understanding and enhancing the safety of next-generation offshore wind turbines.

The paper is structured as follows: Chapter 2 will provide an overview of the theory used throughout this paper. Chapter 3 will delve into the convergence study, where the models will be benchmarked. Chapter 4 will explain the methodology, setup and results of the load comparison. Chapter 5 will present the discussion, and lastly, Chapter 6 will go into the conclusion.

2

Review of Theory

This chapter aims to review the most important theory used in this paper. Section 1 will look into wave loading. Section 2 shows the approaches to wave modelling. And lastly, Section 3 will explain the numerical models.

2.1. Wave Loading

Before delving into the intricacies of calculating wave loads, first, the structure must be known. The most prevalent structures to house wind turbines at the moment are jackets and monopiles. Jackets are steel lattice structures that provide support for offshore wind turbines. These foundations are suitable for a broad range of water depths, making them the preferred choice when the seabed conditions or depth pose challenges for monopile installations. Monopiles involve a single large steel tube driven into the seabed. They are cost-effective, easier to fabricate and straightforward to install. This simplicity makes them the preferred option for installation. This can also be seen in the fact that in Europe, more than 80% of the substructures are monopiles, with the rest being jackets, tripods, and gravity foundations (Vázquez et al., 2022). An overview of substructures can be seen in Figure 2.1, with the structures being, from left to right, the monopile, tripod, jacket, tension leg, gravity-based, and floating support structures.

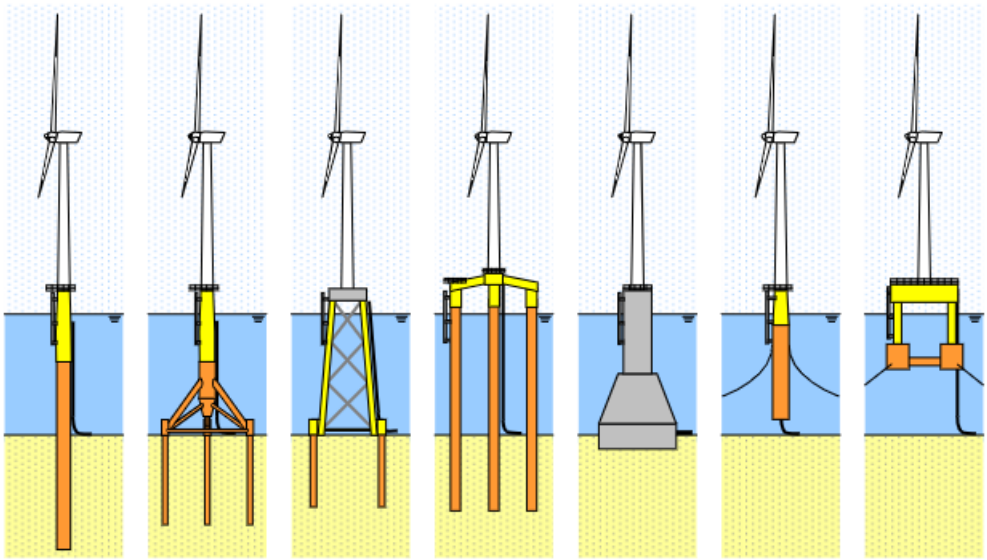

Figure 2.1: Common turbine support structures, as seen in Everen De Vries and Vorpahl, n.d.

In this research, the monopile will be used as the preferred support structure due to it being the most prevalent structure. The monopile can be modelled as a large cylinder, which also introduces

ease of calculation.

There are multiple ways to calculate wave loads acting on structures. While they share some similarities, each method uses a different approach, albeit slight, to account for the various factors that influence wave loading. As mentioned in the introduction, the chosen method is to calculate the wave force using the kinematics and not directly from cell pressure.

The most well-known method is the Morison equation. The Morison equation is a widely used method, introduced by Morison et al., 1950, for calculating wave loads on offshore structures. The equation has been modified over the years to improve accuracy, for instance, by Manners W. and Rainey R.C.T., 1992. The Morison equation can be used with both linear and non-linear theory. When linear wave theory is used, the assumption is made that the waves are small in relation to the size of the structure. It considers two main components of wave loading: the drag force and the inertia force. The drag force is caused by the flow of water around the structure, and the inertia force is due to the acceleration of water particles caused by the motion of the structure. The Morison equation for a cylinder is expressed as:

$$F(t) = F_D(t) + F_I(t) \tag{2.1}$$

Where

$$\begin{aligned} F_D &= \frac{1}{2}\int_{-h}^{\eta} \rho C_D D u|u| dz \\ F_I &= \frac{\pi}{4}\int_{-h}^{\eta} \rho C_M D^2 \dot{u} dz \end{aligned} \tag{2.2}$$

With F representing the total inline force, C_D the drag coefficient, C_M the added mass coefficient, D the cylinder diameter, and $u(t)$ the velocity profile. Using the Morison equation, the mudline moment can easily be determined by multiplying the force times the length between mudline and the midpoint of dz.

Determining the applicability of the Morison equation involves identifying whether the structure lies within the Morison, Froude-Krylov, or diffraction regime. Classification criteria, often based on ratios of wave height to pile diameter and pile circumference to wavelength, assist in regime identification. These criteria are visualised in Figure 2.2, created by Chakrabarti, 1987.

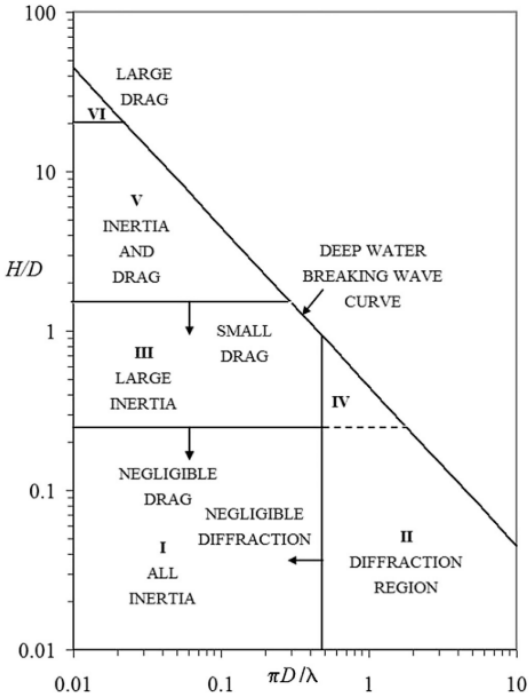

Figure 2.2: Wave forcing regimes by Chakrabarti (1987).

If waves end up in the diffraction region, a diffraction correction is necessary. Wave diffraction occurs when waves encounter a structure, like a monopile, and change direction as they pass around it. The way this works is that when waves approach, for instance, a monopile, they are partially reflected and transmitted by the structure. The reflected waves bounce back and interfere with the incoming waves, causing variations in the amplitudes and directions. The transmitted waves pass through the structure and continue their original path, but their amplitude and direction are also affected. Diffraction can cause large variations in wave loads, leading to increased damage. Therefore it is important to correct these effects using the MacCamy-Fuchs correction. (Schløer et al., 2016)

More specifically, the inertia coefficient needs to be corrected to account for the impact of wave diffraction around the structure. Diffraction causes changes in wave height and direction, affecting the motion and acceleration of the water surrounding the structure. These changes must be factored into the inertia coefficient to ensure accurate predictions of wave loads on the structure (MacCamy and Fuchs, 1954).

The diffraction effects become significant when $\pi D/\lambda > 0.2$, where D is the pile diameter, and λ is the wavelength.

In addition to using the classification chart, the Keulegan-Carpenter number, defined as $K_C = \frac{VT}{D}$ (where V is the flow oscillation velocity and T the period), should be considered. This dimensionless number indicates the relative significance of drag versus inertia forces on submerged objects. With $K_C < 6$, inertia dominates; for $K_C > 60$, drag prevails. This transition from drag to inertia dominance is also depicted in Figure 2.2, transitioning from region VI to I.

2.2. Wave Modelling

There are different ways to tackle the challenge of wave modelling; an overview can be seen in figure Figure 2.3; the different techniques are plotted with the accuracy on the y-axis and the computational time on the x-axis. The most obvious one is experimental modelling; a well-known onshore example is, for instance, the Østerild test centre from the DTU, where 9 test turbines are located. Here one can get real-world data on how the turbines react to wind. Another way to experimentally model turbine behaviour is through placing scale models in basins; a well-known basin is the Delta basin from Deltares- a 250-square-meter pool wherein different types of waves can be modelled. Here, one can check the three-dimensional loads on structures from varying wave directions. For more extreme loads, a wave flume can be used; here, 4,5-meter waves can be modelled in a flume extending over 300 meters. Of course, 4,5 meter high waves are not enough to comply with the most extreme waves in the sea, but one can use scaling to simulate these waves on smaller structures and extend their forces to a full-size model. Experimental modelling is intricate, expensive and unsuitable for calculating load cases to certify wind turbines. However, it has been commonly used to verify quicker computational methods or theories to see if they align with real-world responses.

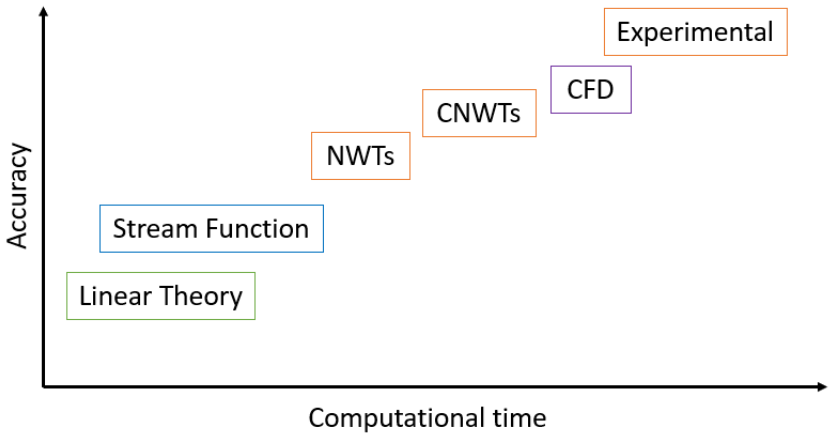

Figure 2.3: Broad overview of different techniques to model wave loads

One of these techniques is computational fluid dynamics (CFD); CFD uses numerical analysis and data structures to solve complex gas- or liquid flows. What makes CFD special is that it can model very intricate waves, such as overturning breaking waves. It can capture wave dynamics and shape with great accuracy and is thus not limited to a single-valued free surface in space (Vyzikas et al., 2021). But with great accuracy and high resolution comes a very high computational cost. This makes such models only applicable to R&D and academic studies. Paulsen et al., 2014 created a method wherein they used another computational method, the so-called numerical wave tank and combined it with a small CFD domain where resolution mattered, denoted in Figure 2.3 as a CNWT. The CPU time for such an operation on medium resolution ranges from 21 to 72 hours. If one were to calculate and certify an entire field of turbines, one would need a simpler theory.

The simplest of theories is linear wave theory, also known as Airy wave theory. Linear wave theory uses a potential flow approach to describe the motion of waves on a fluid surface. It is the fastest way to model waves, but it has many drawbacks, the main one being the inability to handle waves that become non-linear due to asymmetry and steepness. Horizontal asymmetry or skewness is characterized by elongated troughs and shorter, higher crests. Additionally, as waves continue to evolve, especially nearing the point of breaking, they exhibit a forward pitching of the crests, known as vertical asymmetry. Both these asymmetrical shapes result, for instance, from nonlinear triad interactions, where energy is transferred among different wave components. These changes in waveforms are illustrated in Figure 2.4.

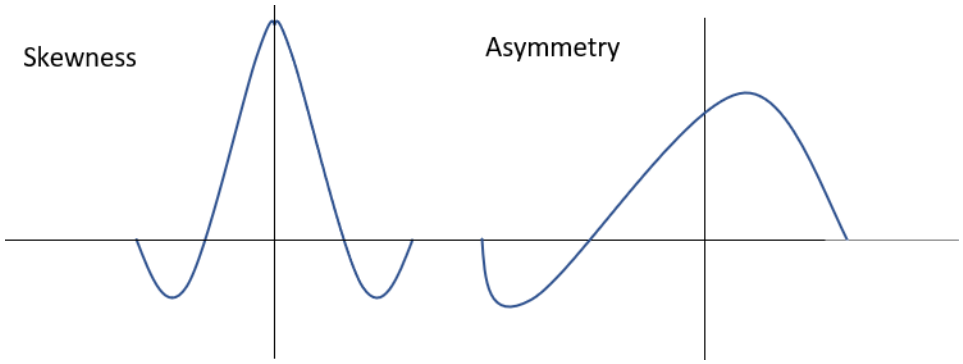

Figure 2.4: Schematic view of wave skewness and -asymmetry

Quantitatively, skewness and asymmetry are calculated based on the free surface elevation η, averaged over time. Asymmetry is derived using the Hilbert transform H of the free surface elevation. The formulas for these calculations are:

$$Sk = \frac{|\eta^3|}{|\eta^2|^{(3/2)}}$$

$$As = \frac{|H(\eta)^3|}{|\eta^2|^{(3/2)}}$$

Where η is the mean water level, and (||) indicates averaging over the time series. For sinusoidal waves, both skewness and asymmetry values are approximately zero.

An overview of when to use which wave theory can be seen in Figure 2.5, created by Le Mehaute, 1976. Here a range of applicable wave theories is shown for a combination of the dimensionless wave steepness and the dimensionless water depth. As can be seen, the linear theory is only applicable to a small range of values. Another method is the stream function method, as established by the work of Fenton and Dean (Fenton, 1988, Dean, 1965), and as standardized in the industry according to the IEC, 2019. It offers a robust approach to tackling the fully non-linear water wave problem. This method stands out for its ability to compute a series solution to this problem by employing the Laplace equation under constraints of constant pressure and specific height. This approach remains valid for a great range of sea states. As shown in Figure 2.5, the stream function is valid up to higher steepness. This combination works by embedding steep waves generated by the stream function into linear wave theory. This embedding process is described in work by, for instance, Suja-Thauvin et al., 2018.

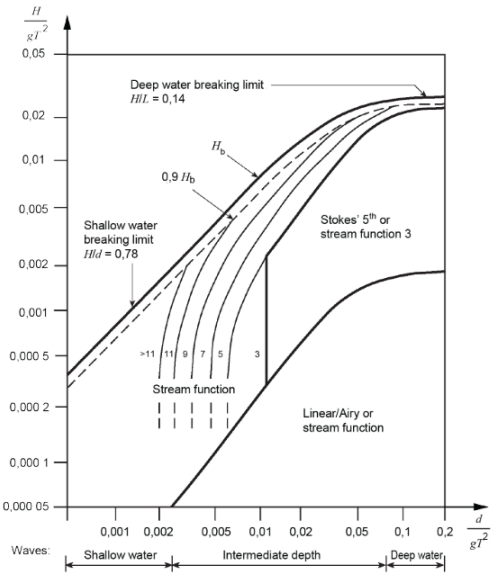

Figure 2.5: Applicable wave theories, summarised by Lè Mèhautè

The benefits of this combination of different theories are that they can be simple in implementation, give fast calculations, and have limited complexity. Moreover, this is beneficial due to the increasing number of simulations needed for turbine certification. However, it has been shown by Peeringa, 2004 that the stream function underestimates breaking wave loads. Therefore it can be considered inaccurate to calculate ultimate strength- and fatigue-load cases when, for instance, steep waves from storms are considered. An explanation for this inaccuracy could be the large number of assumptions made in this theory. For example, it has 2D motion, considers flat beds, symmetry around the crest and a constant wave shape. An example of the embedding process and the wave shape can be seen in Figure 2.6.

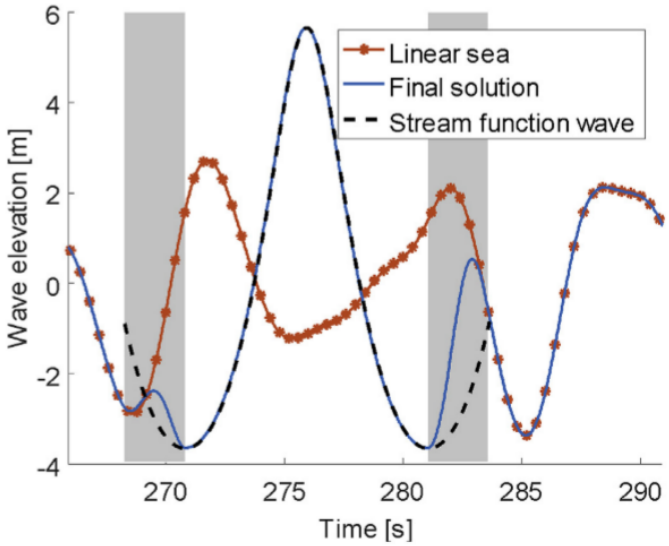

Figure 2.6: Embedding of a wave as shown by Suja-Thauvin et al., 2018

Another method which has shown great potential in recent studies by, for instance, Wang et al., 2021, is the numerical wave tank (NWT). Numerical wave tanks provide fully non-linear wave models using a range of theories. Such non-linear models are an order of magnitude faster than CFD but intrinsically account for the non-linear effects of waves resulting in asymmetric wave shapes. As such, they are expected to provide more realistic predictions of the storm wave loads compared to industry

standards. However, one significant drawback of these models is that they only account for a single value in space on the free surface. Thus, they will not be able to model overturning waves. These models will be explained in the upcoming section.

2.3. Numerical Models

Many numerical wave models exist, all with a range of different underlying theories and functionalities. In this research, SWASH and OceanWave3D will be used; these are explained below.

2.3.1. SWASH

The first model considered is SWASH (Simulating WAves till SHore). SWASH is an open-source model developed at the Technical University of Delft by Zijlema et al., 2011b. SWASH is a deterministic time domain phase resolving wave model based on non-linear shallow water equations with added non-hydrostatic effects. SWASH is mainly used for coastal engineering problems but can also be applied to large-scale ocean applications. The 1D depth-averaged, non-linear shallow water (NLSW) equations in the non-conservative form are shown as follows:

$$\begin{aligned}
&\frac{\partial \zeta}{\partial t} + \frac{\partial hu}{\partial x} = 0 \\
&\frac{\partial u}{\partial t} + u\frac{\partial u}{\partial x} + g\frac{\partial \zeta}{\partial x} + \frac{1}{2}\frac{\partial p_b}{\partial x} + \frac{1}{2}\frac{p_b}{h}\frac{\partial(\zeta - \mathsf{d})}{\partial x} + c_f\frac{u|u|}{h} = 0 \\
&\frac{\partial w_s}{\partial t} = \frac{2p_b}{h} - \frac{\partial w_b}{\partial t} \\
&w_b = -u\frac{\partial d}{\partial x} \\
&\frac{\partial u}{\partial x} + \frac{w_s - w_b}{h} = 0
\end{aligned} \tag{2.3}$$

Where ζ is the free surface elevation, t is time, h is the total depth, u is the depth-averaged velocity, and x is the horizontal coordinate. Furthermore, d is the still water depth, p_b is the non-hydrostatic pressure at the bottom, g is the gravitational acceleration, and c_f is the dimensionless bottom friction coefficient. The bottom friction coefficient can be calculated in multiple ways and is used to increase numerical stability; one of the methods to calculate bottom friction is by using Manning's roughness coefficient n as follows:

$$c_f = \frac{n^2 g}{h^{1/3}} \tag{2.4}$$

In Equation 2.3, the first and last equations are the global and local continuity equations, which ensure local and global mass conservation. The second equation is the momentum equation for the u-velocity, including the bottom friction and the effect of non-hydrostatic pressure. The third equation is the momentum equation for the vertical velocity at the free surface, w_s. The fourth equation states the velocity at the bottom, w_b, described by the kinematic condition presented as the last equation. An important thing to note is that SWASH is based on the incompressible Navier-Stokes equations, where multiple layers in the vertical direction are considered.
SWASH was developed because, at the time, the other models were mainly based on the Boussinesq equations, where artificial methods were implemented to account for wave breaking. For instance, by monitoring the upward particle acceleration and filtering the wave when it exceeds a certain limit. These artificial methods are used due to Boussinesq-type wave models' inability to conserve momentum due to frequency dispersion and non-linearity. Furthermore, these models, such as Mike 21 BW and BOUSS-2D, contain tunable parameters to onset breaking. This makes their performance of variable quality (Zijlema et al., 2011a).

SWASH offers an alternative solution to solve wave breaking. It has been shown to accurately predict the onset of the breaking process and the amount of energy dissipation in the surf zone. This is achieved by modelling breaking waves as moving Rankine-Hugoniot jumps while preserving the asymmetry and skewness of waves (Zijlema, 2019).

Mentions in literature

SWASH has been around since 2011 and has been validated and used extensively; most of its research focuses on coastal areas. The most interesting papers for this report are the ones concerning wave breaking. Zijlema and Stelling have done multiple of these, showing accurate results (Smit et al., 2013; Stelling and Zijlema, 2009).

SWASH has also been compared to several numerical models, for instance, with MIKE21 by Roo et al., 2015, where it was found that the results aligned, but SWASH was more robust. Another study done by Vyzikas et al., 2021 compared OpenFOAM (an open-source CFD program), SWASH and HOS-NWT. It was shown that SWASH and HOS-NWT performed well in capturing interactions up until the fifth order. Moreover, SWASH and HOS-NWT even outperformed OpenFoam in capturing higher-order individual harmonics. Furthermore, SWASH converged for multiple combinations of parameters while balancing accuracy and computational efficiency.

Wave generation

SWASH has multiple ways to set up wave generation, for instance, by applying either a Pierson-Moskowitz or JONSWAP spectrum. The latter will be used in part 2 of this research. Additionally, boundary conditions can be established, with wave input facilitated through a velocity distribution at the inlet boundary. In this research, a weakly reflective condition will be implemented, wherein the velocity is imposed using a vertical hyperbolic cosine. Finally, a smoothing function is applied to initiate the simulation smoothly, a ramp-up time.

Numerical setup

In numerical modelling, particularly in the simulation of wave dynamics, discretization is a crucial step that involves approximating continuous mathematical models to a discrete set for computational simulation. In SWASH, various schemes can be employed for this purpose, including the First Order UPWind, Higher Order UPWind with the κ formulation, BDF (Backward Differentiation Formula), MUSCL (Monotonic Upstream-centered Schemes for Conservation Laws), and many more. These schemes all have their own drawbacks and benefits. The numerical schemes for this paper can be seen in Table 2.1

Table 2.1: Discretization of the advection terms used in the momentum equations.

Term	Scheme	Order
$u\frac{\delta u}{\delta x}$	UPW	MSCL
$u\frac{\delta w}{\delta x}$	UPW	FIRST
$w\frac{\delta u}{\delta x}$	UPW	MUSCL
$w\frac{\delta w}{\delta x}$	UPW	FIRST

All directions employ the Upwind discretization scheme, chosen due to its stability and ability to handle steep gradients and discontinuities. The scheme complies with the Rankine-Hugoniot jump relations and is specifically designed to preserve local momentum flux. Thus it is crucial for the simulation of breaking waves and unsteady bores. The MUSCL scheme is used in the horizontal direction, and the first-order scheme is used in the vertical. This is because the First-order scheme is better at dealing with sharp gradients and discontinuities without introducing spurious oscillations. MUSCL is used in the horizontal direction due to the fact that the horizontal direction has more grid points and can thus accommodate a more complex scheme. Furthermore, steep waves have more pronounced features due to, for instance, breaking and shoaling. Utilising such a scheme in the horizontal direction allows for a better capture of these dynamics, along with a decrease in numerical diffusion. The vertical features will undergo discontinuities, especially with breaking waves, so it is important to have a scheme which can handle those discontinuities. More details about these schemes can be found in the SWASH user manual by Zijlema, 2010.

The time integration method is explicit using the leapfrog scheme; in explicit time integration, the time step is based on the Courant condition (Cr) for stability; the formula is as follows:

$$Cr = \frac{\Delta t(\sqrt{(}gd) + \sqrt{(}u^2)}{\Delta x}$$

Where u is the flow velocity in the horizontal direction, Δt is the time step, and Δx the spatial step or resolution. A maximum courant number of 0.5 is advised for high waves, nonlinearities and surface

interactions. Zijlema, 2010 If Cr exceeds the preset limits, the timestep is halved to ensure stability. For this research, the limits are kept between 0.2 and 0.5. In part 1 of the research, the limits are set to 0.01 and 1 to ensure the timestep stays equal for a fair comparison.

Lastly, SWASH allows its users to include the non-hydrostatic pressure in the shallow water equations through a command. Not including it is useful when looking at large-scale ocean circulations, tides and surges. For this research, the aim is to analyse single waves in detail, so the non-hydrostatic pressure term will be included. Two schemes can be chosen to handle the vertical pressure gradient, a classical central differencing scheme and the Keller-box scheme. The Keller-box scheme with an implicit Euler method is used for this research because it is the method for accurate short-wave propagation. Where the central differencing scheme is, for instance, used in cases with stratified flows and undertow. For this scheme, preconditioners can be used to accelerate the convergence of iterative methods; in SWASH, the choice can be made between ILU and ILUD, where ILU stands for the incomplete LU factorization, and ILUD is a modified version suited for parallel computing. ILU is more robust and is thus implemented in this research.

2.3.2. OceanWave3D

OceanWave3D (OW3D) is a fully non-linear potential flow solver for large-scale wave propagation developed by Engsig-Karup et al., 2009. Its key features include that it has no depth limitations, is open-source, and can be used in both 2D and 3D. Applications include wave propagation and transformation, wave loads on slender structures, and the use of it as a numerical wave tank. OW3D is developed as a fully non-linear flexible-order potential flow solver, which can describe the propagation and development of 3D non-linear waves up to the point of breaking. Like Bousinessq models, OW3D has an extra function that ensures the numerical solver's robustness if it encounters breaking waves, it does not attempt to model breaking waves, but it ensures numerical robustness and stability by using a threshold and then applying a compact spatial filter (Paulsen et al., 2013).

OW3D can be described by solving the Laplace equations for the velocity potential. An overview of the full equations can be found in papers released by Engsig-Karup et al., 2012. Below, the simplified relations for a 2D model are given, taken out of work by Pavilons et al., 2022. These equations are based on the premise of potential flow, which entails that the flow is irrotational and incompressible. First off, the velocity potential relates to the fluid velocities in the following way:

$$\mathbf{u} = \nabla * \phi \tag{2.5}$$

Where ϕ is the velocity potential, **u** is the velocity vector and ∇ the differential operator. These are given as follows.

$$\mathbf{u} = (u_x, u_z) \tag{2.6}$$

$$\nabla = \left(\frac{\partial}{\partial x}, \frac{\partial}{\partial z} \right) \tag{2.7}$$

These lead to the kinematic free surface condition as noted by Paulsen et al., 2014, which is stated as:

$$\frac{\partial \eta}{\partial t} = -\frac{\partial \eta}{\partial x}\frac{\partial \tilde{\phi}}{\partial x} + \frac{\partial \tilde{\phi}}{\partial z}\left(1 + \left(\frac{\partial \eta}{\partial x}\right)^2\right) \tag{2.8}$$

η is the free surface elevation, and t is time. The velocity potential is described in the following way:

$$\tilde{\phi} = \phi|_{z=\eta} \tag{2.9}$$

The dynamic free surface condition, also taken from Paulsen et al., reads:

$$\frac{\partial \tilde{\phi}}{\partial t} = -g\eta - \frac{1}{2}\left(\left(\frac{\partial \tilde{\phi}}{\partial x}\right)^2 - \left(\frac{\partial \tilde{\phi}}{\partial z}\right)^2\left(1 + \left(\frac{\partial \eta}{\partial x}\right)^2\right)\right) \tag{2.10}$$

Where g is the gravitational acceleration; furthermore, what is important to note is that these equations have been set up using a no-penetration boundary condition.

OW3D uses fast Fourier transforms and scales with $O(n)$ and thus uses very little computational time. OW3D has been validated extensively and used in multiple analyses by, for instance, Schløer et al., 2016; Wang et al., 2021.

The main limitation OW3D has is that for steep waves, the theory breaks down; breaking or unstable waves are thus often observed as discontinuities because of filtering. What happens is that as the wave approaches its overturning point, the wavefront becomes steeper. This means the local wave steepness $\left(\frac{\partial \eta}{\partial x}\right)$ approaches negative infinity before overturning. This generates an infinite surface elevation growth rate $\left(\frac{\partial \eta}{\partial t}\right)$ (Pavilons et al., 2022). This is noted in the following way:

$$\lim_{x \to -\infty} \frac{\partial \eta}{\partial t}\left(\frac{\partial \eta}{\partial x}\right) = \infty \frac{\partial \tilde{\phi}}{\partial x} + \infty^2 \frac{\partial \tilde{\phi}}{\partial z} \tag{2.11}$$

A way to circumvent this limitation is to apply filtering to ensure numerical stability. In OW3D, this is done by controlling the maximum vertical acceleration, which by default is set to 0.5 times the gravitational constant. Pavilons et al., 2022 goes into depth by trying to come up with a new breaking criterion; this is done by coupling OW3D to the CFD toolbox OpenFOAM. Using OpenFoam, a new kinematic breaking criterion is determined; it is advised to keep the user-defined breaking parameter for OW3D at 1. The same goes for the paper by Varing et al., n.d.; in this paper, they numerically investigate the validity of the breaking criterion for fully nonlinear potential flow solvers. The same conclusion is drawn here: the criterion should be set to 1.

Mentions in literature

OW3D has been mentioned extensively in literature; some crucial findings include the study of Wang et al., 2021, where OW3D was used to perform an ultimate load analysis on a 10 MW offshore monopile wind turbine. This study ran simulations for a 10MW turbine in parked and operational conditions, using linear, constrained and non-linear waves.

Other important findings include research by Paulsen et al., 2013, where it was shown that OW3D could reproduce the wave transformations, free surface elevation and inline forces with good agreement. However, it was again shown that force was more accurately captured using CFD models for the steepest near-breaking waves. It was also mentioned that combining OW3D with OpenFoam would be a promising way to calculate offshore wave loads, which the same researchers also did (Paulsen et al., 2014).

An example of a direct comparison between OW3D and SWASH can be found in the literature by Düz et al., 2016. Here, an inventory study has been done to compare the functionalities of the two. However, to the best of the author's knowledge, no direct comparisons have been made to determine the quantitative difference in terms of speed, accuracy and convergence.

Wave generation

OW3D allows for multiple ways to apply wave generation. Like SWASH, it allows for input of a JONSWAP or Pierson-Moskowitz (PM) spectrum or for a velocity distribution at the inlet boundary. Next to these three methods, it also allows for input by stream function. Spectrums like JONSWAP or PM will have to be applied by using a wave generation zone, unlike SWASH, where it is all applied at the inlet boundary. To comply with this limitation, the length of the OW3D tank is increased by two wavelengths to allow for proper generation time and length. Just like SWASH, OW3D also allows for smoothing due to the application of ramp time.

Numerical setup

Spatial discretization in the domain is done using the finite difference method at the domain's boundaries, the bottom and side walls, Neumann is imposed (Engsig-Karup et al., 2009). OW3D does not allow for much altering of numerical schemes; the inputs that can be changed are the alpha, beta and gamma values in the finite difference method and their respective preconditioners. For the time integration of the free surface conditions, the explicit four-stage, fourth-order Runge-Kutta scheme is used. OW3D uses a different formulation for the courant number,

$$Cr = \frac{\Delta t \sqrt{u^2}}{\Delta x}$$

.

3

Numerical Analysis

In the pursuit of high-fidelity simulations, grid resolution plays an important role as it directly influences the level of detail at which the wave phenomena are captured. Higher grid resolution generally leads to enhanced accuracy in the simulated wave fields, allowing for the intricate details of wave dynamics to emerge. However, this increased precision comes at the cost of computational resources. As the grid resolution is refined, the number of calculations required increases exponentially, demanding more computational power and time.

Achieving the right balance in grid resolution is, therefore, a delicate optimization problem. It involves finding a grid that is fine enough to capture the essential physics without being so fine that the computational load becomes untenable. The key is to enhance resolution up to the point where further refinement does not yield significant improvements in simulation accuracy. This convergence study systematically explores this balance, seeking the sweet spot where the benefits of higher resolution begin to level off, and the computational expenses continue to rise sharply.

This Chapter is divided into three parts. First, it goes into the methodology to highlight the details of both the convergence study and the computational efficiency test. Secondly, it will go into numerical wave tank setup, and lastly, the results will be displayed.

3.1. Methodology

3.1.1. Convergence Study

The convergence study's objective is to identify the resolution at which numerical solutions approach a sufficiently accurate representation of the physical wave phenomena under study. Below a step-by-step approach for the convergence study can be seen:

- Start with a coarse resolution, so a low amount of grid points per wavelength.
- Incremental increase of the resolution to determine the sensitivity to resolution changes.
- Compare the recorded wave data to a reference solution, in this case, the highest resolution in the set.
- Identifying the point of diminishing returns to ensure that computation resources are not wasted on over-refining the grid.

The sensitivity will be determined by looking at the amplitude- and phase errors. An example of these errors can be seen in Figure 3.1. Where the amplitude error is shown in the plot on the left, and the phase error is shown in the plot on the right. The differences for the amplitude and phase are denoted as ΔA and $\Delta \phi$. The error is calculated as:

$$\epsilon_{amp} = mean(\frac{amplitude_{actual} - amplitude_{ref}}{amplitude_{ref}})$$

$$\epsilon_{phase} = mean(\frac{phase_{actual} - phase_{ref}}{phase_{ref}})$$

Where the reference amplitude is the mean amplitude of the experiment with the highest resolution, and the actual amplitude is the mean amplitude for any of the experiments in the set. The mean is taken over 50 waves. The waves will be monochromatic, and the amplitude and phase will be calculated using a fast Fourier transform (FFT), which transforms the signal from the time domain to the frequency domain. Bracewell, 2000 Using this analysis, the amplitudes and accompanying phases can be calculated in detail. The FFT is used because it makes it easier to check for the presence of, for instance, non-linear components to the signal. It is a check to see if it is purely linear. This error will be analysed for both the x- and z-direction. To start, the resolution in the x-direction will be fine-tuned; this test seeks to find the point where increasing the resolution no longer leads to significant gains in terms of error. These errors arise due to the numerical dispersion seen with, for instance, coarse grids.

Numerical simulations employ grids to discretize the domain, enabling the representation of physical phenomena through computational methods. Coarse grids introduce errors in amplitude by inadequately capturing the details of the underlying physics. Numerical dispersion on coarse grids leads to an inaccurate representation of wave propagation, causing the simulation to deviate from the true behaviour observed in experiments.

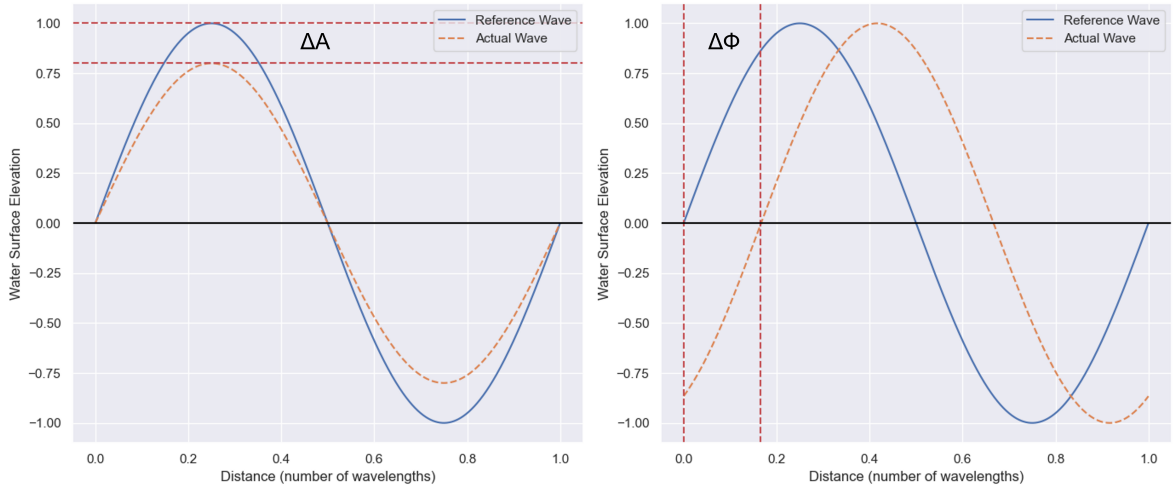

Figure 3.1: Amplitude and Phase error for a sinusoidal signal. The dotted lines show the error.

Errors found in these simulations are generally low, especially for OW3D since it is a fourth-order model, with swash being a second-order model. For this study, the timesteps are kept so that the Courant number stays stable. Having a benchmark for both models with linear settings gives a solid start to figuring out the correct settings for non-linear waves. Furthermore, it provides a baseline comparison for both models.

3.1.2. Computational Efficiency

Next to accuracy, speed per timestep or computational efficiency is also a vital part of this convergence study. To address this, a comparative analysis of computational speed is conducted. The approach for this test is approximately the same as the approach for the convergence study; the difference is that it will be looking at the computational time as a fraction of the simulation time. Where the simulation time is the set time of the experiment, for instance, a one-hour sea state, and the computational time is the real-world time the simulation takes. A fraction of 0.5 would mean that a one-hour sea state would take 30 minutes of real-world time to solve.

Once again, we can look at the point of diminishing returns and keep a certain computational efficiency to ensure practicality. The steps taken are summarised below.

- Start with the values found in the convergence study, so the optimal x- and z-resolutions.
- Add an incremental increase and decrease in the x- and z-directions.
- Calculate the computational time taken per timestep and look at the difference between SWASH and OW3D.

- If clear benefits can be seen in differing the number of gridpoints, change the settings.

By systematically evaluating the trade-offs between resolution and computational resources, this research will contribute to more sustainable and rational use of high-performance computing resources in wave modelling, which is of significant importance given the time-intensive nature of large-scale simulations.

3.2. Numerical Wave Tank setup

The setup for the tests described is as follows:

- Both NWTs are set to 2D vertical (2DV).
- The bathymetry is flat, and the depth is set to 30 meters.
- Wave generation for SWASH is done by imposing a velocity distribution at the boundary, for OW3D it is done by imposing a stream function in a generation zone.
- The length of the wave tank is based on the wavelength; the lengths for swash and ow3d are 9 and 11 wavelengths, respectively. OW3D has two extra wavelengths due to the generation zone.

A schematic overview of the wave tank can be seen in Figure 3.2, where the regions are labelled, and the positioning of the wave gauge is shown. This overview also highlights the sponge layer; this layer is used to dampen the wave completely to make sure there is no reflection. Lastly, the error is taken after a certain T_{steady} to ensure steady waves reach the wave gauge. T_{steady} is quantified as the time it takes for the waves to reach the wave gauge.

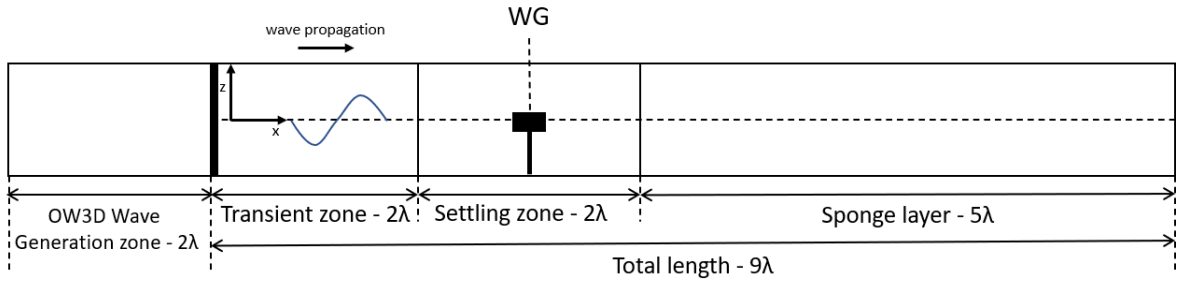

Figure 3.2: Numerical wave tank overview, wave gauge placed at 3λ

OW3D does not account for bottom friction; the bottom friction in SWASH is calculated using the Manning roughness coefficient and can be seen as negligible. The error calculated in this section is thus mainly due to numerical effects such as truncating errors.

An overview of all inputs for the convergence study is summarised below:

- H_s is set to $0.01m$ for both models; Tp has the following values; 7.92, 18.1 and 33.6.
- The number of gridpoints per λ for the x-direction ranges from $9 - 243$, where the steps increase exponentially over the amount of simulations with the following relation $last\_gridpoints + n * 3$.
- For the z-direction, the number of gridpoints per λ ranges from $8 - 20$ with steps of 2.
- The depth is set to $30m$, which results in the following kd values, $0.33, 0.65$ and 2.00.
- Lastly, the runtime for both simulations is set to 50 waves, and the errors are averaged over these 50 waves.

For the test in computational efficiency, most of the values are the same; the only difference is in grid points for both directions. These are as follows;

- For the x-direction, they vary from the number set by the convergence study with $+ - 18$ points and in the z-direction, they vary with $+ - 4$ layers.

3.3. Results

3.3.1. Convergence Study

Below in Figure 3.3 and Figure 3.4, the results for the convergence study in the x-direction are shown. On the x-axis, the number of grid points per wavelength, also known as the x-resolution, is shown. On the y-axis, the relative error in percentages is shown; both axes are on a log scale. Furthermore, the red dotted horizontal line shows the arbitrary set threshold of 0.25%. This value is chosen as it provides a trade-off between resolution and error.

Figure 3.3: Amplitude- and phase error plots for SWASH, the red dotted line indicates an error of 0.25%.

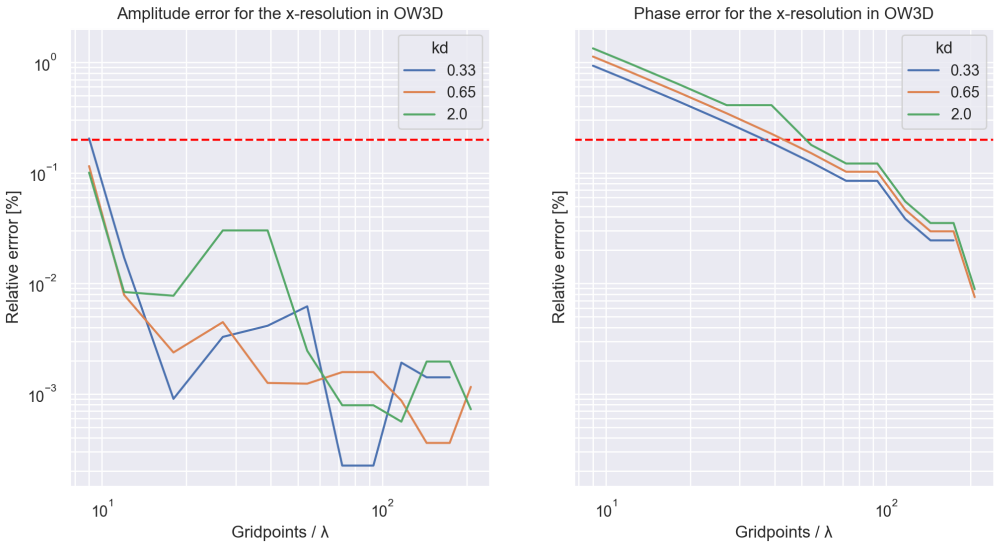

Figure 3.4: Amplitude- and phase error plots for OW3D, the red dotted line indicates an error of 0.25%.

In Figure 3.3 and 3.4, different patterns can be seen in the results. The amplitude errors in OW3D initially fall below the set threshold and gradually converge to an error of 0.001%. Whereas, in SWASH, the errors start at 0.8% and steadily converge to 0.01%. The results for the phase error are different for both, with SWASH starting below the threshold, while OW3D starts above it. Which is the other

way around with respect to the amplitude error. Furthermore, the amplitude errors in OW3D display noticeable noise but do eventually converge.

Based on these results, specific resolutions are proposed for the x-direction in SWASH and OW3D. SWASH will be configured to 100 gridpoints/λ, while OW3D will be set to 57 gridpoints/λ. These determined values will be utilized in the subsequent convergence study conducted in the z-direction, as depicted in Figure 3.5 and 3.6.

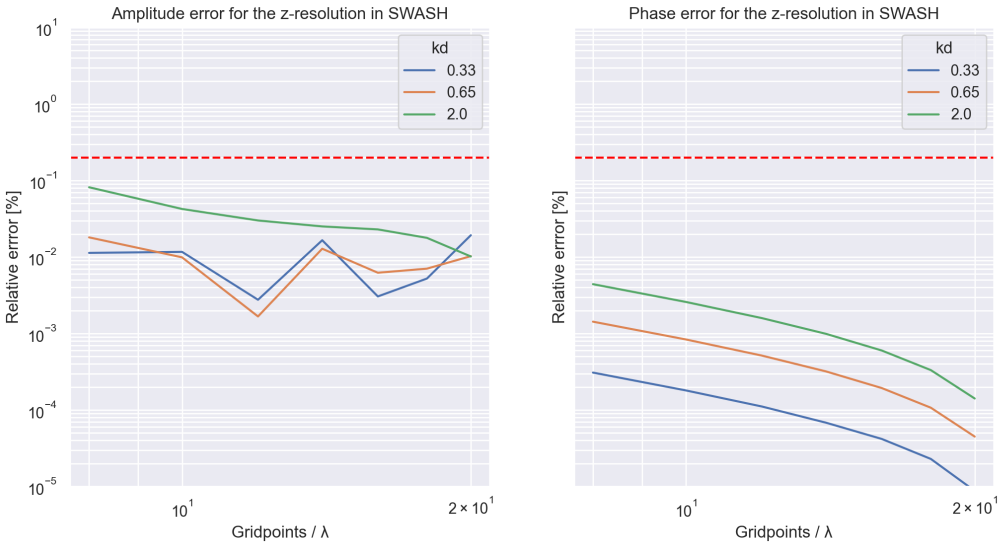

Figure 3.5: Amplitude- and phase error plots for SWASH, red dotted line indicates an error of 0.25%.

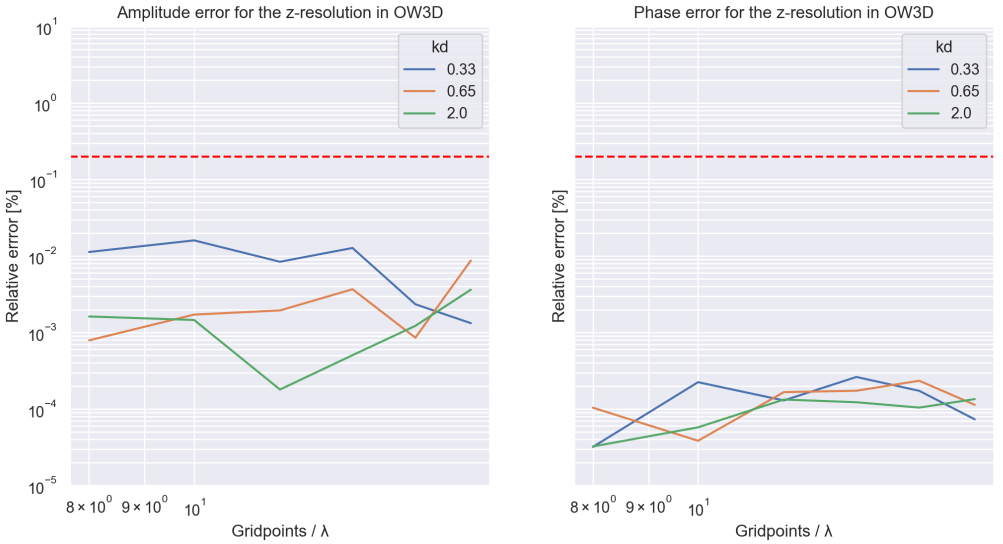

Figure 3.6: Amplitude- and phase error plots for SWASH, red dotted line indicates an error of 0.25%.

The results in Figure 3.5 and 3.6 show the following results. The amplitude errors for SWASH and OW3D hardly converge to lower errors; a few dips can be seen for both models. The errors all start below the set threshold. Furthermore, in the phase errors, a clear convergence can be seen in SWASH, whereas varying the number of layers in OW3D has little effect on the phase error. The phase error in swash lowers due to the fact that when the amount of layers increases, the accuracy of the phase velocity increases. This is due to SWASH using its own dispersion relation, which is an approximation

of the exact linear dispersion relation dependent on the number of layers. This entails that the more layers are used, the more accurate it will be.

The results seen above show that the number of layers does not have to be increased to meet the threshold. This convergence study leads to baseline parameters.

3.3.2. Computational Efficiency

The results for the computational efficiency test can be seen in Figure 3.7 and 3.8. On the y-axis, the fraction of computational time divided by simulation time can be seen. As an example, a value of 0.5 would lead to a computation time of 30 minutes if the simulation time is one hour. As can be seen, the number of layers has a bigger influence on the computational time, as for every extra layer, the grid increases by the number of grid points, whereas increasing the number of grid points only adds to the number of layers. This can also be seen in the figures, as the slope is steeper in Figure 3.8.

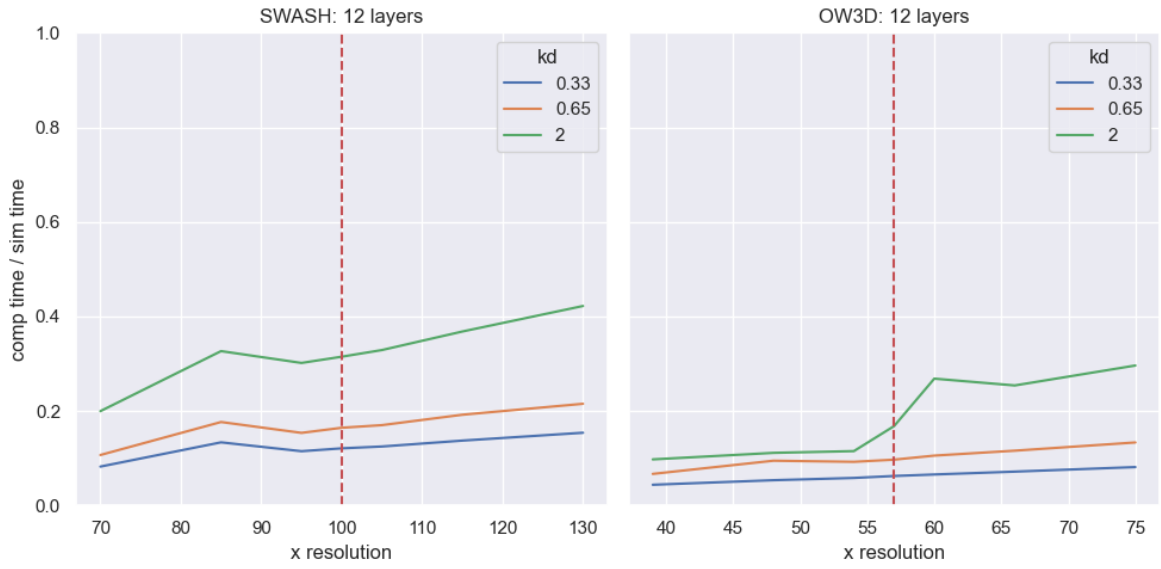

Figure 3.7: Computational time divided by simulation time for both SWASH and OW3D

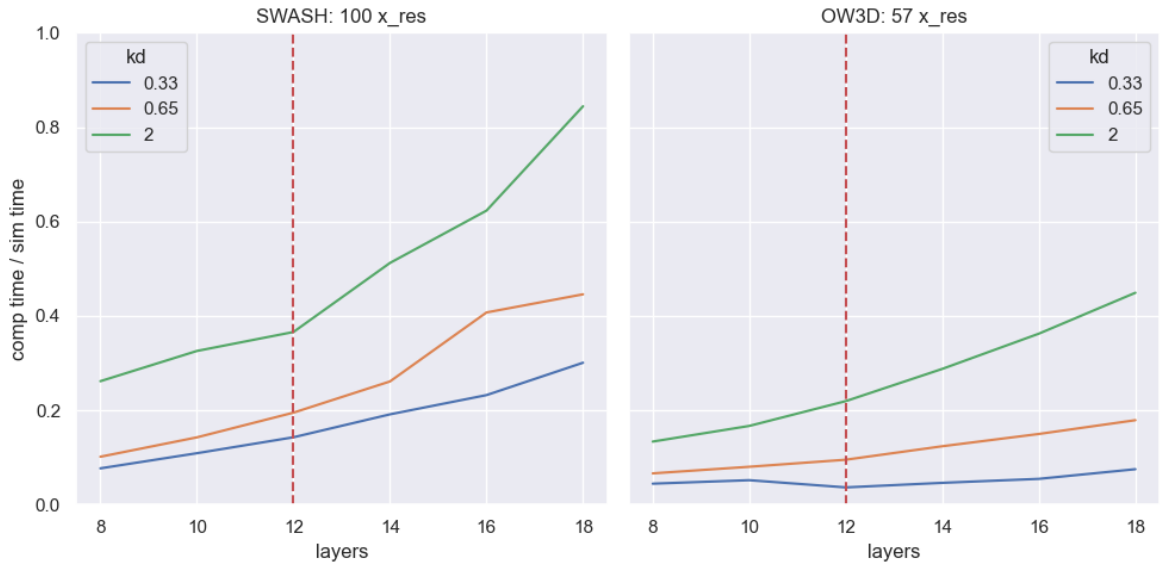

Figure 3.8: Comparison of computational speed per timestep for both SWASH and OW3D

The most important result in the plots above that can be seen is that OW3D shows lower computational time in both the x- and z-direction.

4

Load Comparison

This chapter will go into the load comparison among the three models: SWASH, OW3D, and the Stream Function approach, which has a linear sea state with embedded extreme waves. The comparison aims to understand the differences in the models by analysing the kinematic output. First, a comparison will be made between SWASH, OW3D and linear theory. Compare both models to linear theory to see how non-linear effects influence the output. Furthermore, it will show how both non-linear models differ due to their underlying fundamentals. Second, a comparison will be made between the most extreme waves in SWASH and OW3D and compare those with the extreme waves generated by the stream function. This comparison aims to show if and how the effects introduced by the non-linear models affect the wave shape and influence.

The structure of this chapter is as follows. First, the methodology will be explained, and the setup and choice of parameters will be discussed. Then, the results will be displayed, where distinctions are made between wave spectra and wave statistics for the non-linear models, compared to linear theory, and lastly, the stream function will be compared to the non-linear models, looking at individual wave shapes.

4.1. Methodology

4.1.1. Setup

Before applying the Morison equation to calculate the force on the structure, a check must be done to ensure that the structure is within the Morison regime. A classification has been made by Chakrabarti, 1987 and is stated in Figure 4.1. As can be seen in the figure, the average wave falls into the Morison regime. This is mainly due to the long periods for each wave, which is set to 14 seconds. However, due to the input being a JONSWAP spectrum, the period can differ, so for analysis of the most extreme waves, a check will be done to ensure they fall in the Morison regime. This check consists of calculating $\frac{\pi D}{\lambda}$ to see if it falls below 0.20.

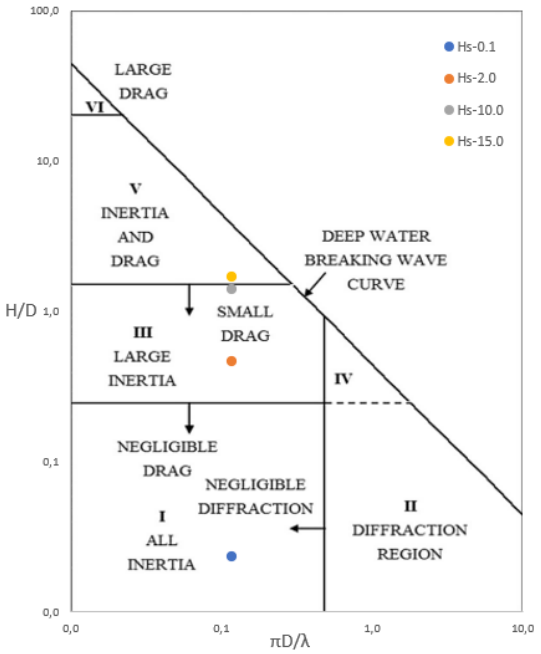

Figure 4.1: Wave diagram where the four cases are highlighted.

For the wave selection, one can use the mehauté diagram; the mehauté diagram shows various wave theories along with their regions of validity. These theories include the linear (or Airy) wave theory and higher-order stokes, among others. The horizontal axis denotes the non-dimensional water depth, h/gT^2. This parameter denotes the relative deepness of the water to the length of the wave. The vertical axis denotes the non-dimensional wave steepness denoted as H/gT^2; here, the H is either the significant wave height H_s or the max wave height based on the rayleigh distribution, $H_{max} = 1.86 * H_s$. The period for H_s is taken as T_p, and the period for H_{max} is taken as the average of the wave period range associated with extreme wave heights taken out of IEC, 2019. Which is defined as; $11.1\sqrt{H_s/g} \leq T \leq 14.3\sqrt{H_s/g}$.

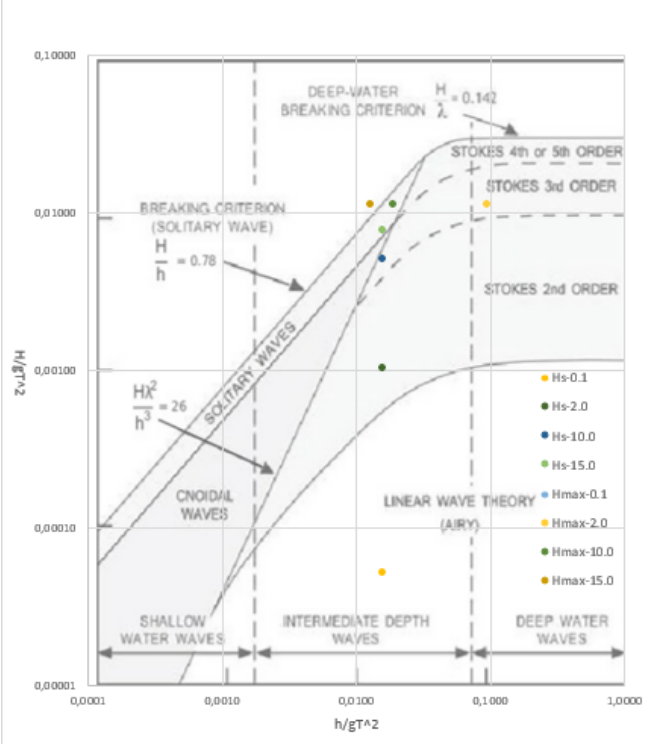

Figure 4.2: mehaute diagram w/ dots for the inputs etc.

The wave parameters are taken so that they can be analyzed in linear and non-linear conditions to see what the influence of non-linearity is on these models. This can clearly be seen in the mehauté diagram presented in Figure 4.2. The most extreme case with an H_s of 15 even contains strong non-linear waves, which represent breaking characteristics.

The wave and force parameters for this study are as follows;

- The amount of layers in the z-direction is equal to 12, and the resolutions for both SWASH and OW3D are 100 and 57, respectively.
- The depth throughout the numerical wave tank depends on H_s; it starts at a certain value and then slopes up steadily with 1:85 to the wave gauge, where the depth is equal to $30m$.
- The significant wave heights are taken as $0.1, 2, 10$ and $15m$.
- The input will be a JONSWAP spectrum with a gamma value of 3.3.
- The duration of the simulations is taken as one hour, with 10 random simulations per case.
- For the monopile, a diameter of $8m$ is used.
- The coefficients for drag and inertia, C_d and C_m, are set to 1.0 and 2.0.

The stream function method can also be used when looking at extreme waves. Therefore, it is only implemented for the case of $H_s = 10$. As this method does not converge above the breaking limit.

4.2. Results

Before looking at the load response, the wave spectra and wave statistics are examined. Not all figures are shown in the upcoming chapters; for a complete overview, one can look at the Appendix. In this section, first, both SWASH and OW3D will be compared to linear theory. Afterwards, they will be compared to the stream function method.

4.2.1. Comparison of SWASH and OW3D

Wave Spectra

The distribution of wave energy is an important parameter in figuring out the structural responses; this is due to the fact that different frequencies of waves can have varying effects on the structure. For instance, when there is energy at the natural frequency of the structure, this can introduce resonance, which may lead to increased structural responses. The wave spectra, as shown in Figure 4.3 and Figure 4.4, show the power spectral density on the y-axis and the frequency on the x-axis. The spectra are shown as ensemble averages, which are averaged over a total of ten realisations. The inputs are, as mentioned, JONSWAP spectra with differing values for H_s. To check for energy loss due to, for instance, wave breaking or numerical errors, the significant wave height can be calculated. The significant wave height is related to the wave spectrum by the following relationship:

$$H_s = 4\sqrt{\int_0^\infty S(f)df} \tag{4.1}$$

Where $S(f)$ is the power spectral density. The calculated values will be shown later on in this chapter in Table 4.1

In Figure 4.3 the response of a linear sea state can be seen, Figure 4.4 shows the response in a non-linear sea state. What becomes apparent when looking at these responses is that for the linear sea state in Figure 4.3, OW3D and SWASH seem to agree in terms of the overall shape. The only difference is that all models show slightly differing shapes at higher frequencies ($f > 0.08Hz$), which include the shorter waves. In Figure 4.4, larger differences can be seen; first off, both SWASH and OW3D show an increase in energy at the subharmonics around $f = 0.015Hz$. Furthermore, at around $f = 0.14Hz$, a slight increase in energy can be seen for both SWASH and OW3D. This energy transfer to sub- and higher harmonics can be attributed to non-linear effects. Where transfer to sub- and higher harmonics can be attributed to triad wave-wave interactions. Lastly, a big decrease in energy at the spectral peak for OW3D can be seen. These simulations do not include wave breaking, so these effects must be attributed to other factors.

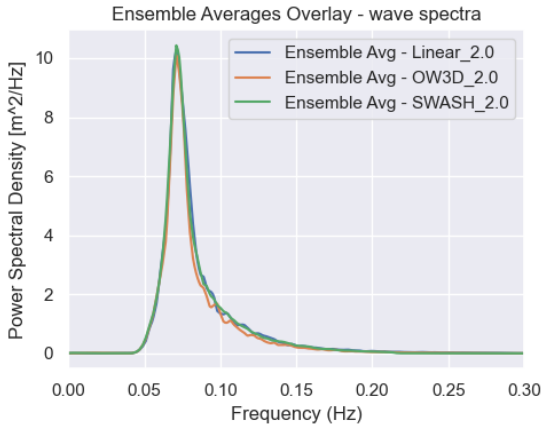

Figure 4.3: Wave spectra for $H_s = 2.0$

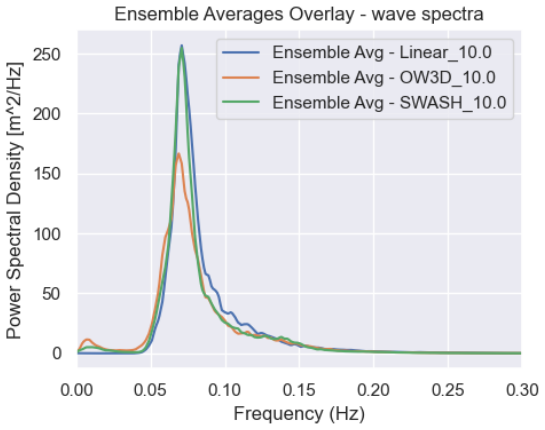

Figure 4.4: Wave spectra for $H_s = 10.0$

Below in Table 4.1, the input and output values can be seen for the simulations shown in Figures 4.3 and 4.4. When looking at the values for OW3D, what becomes immediately apparent is that, for starters, there is a large percentage difference, even for the linear sea states of 0.1 and 2.0. This increases further for the case of $H_s = 10.0$. The height of these errors is out of trend when comparing

them to the other two models. A possible reason for this is that the model is improperly set up, where, for instance, the x-resolution is too low, which in turn leads to discretisation errors. This becomes especially apparent when looking at the value for $H_s = 15.0$, where for OW3D, energy is created. This is not as expected and should not be possible. Which highlights that OW3D is improperly set up. SWASH, on the other hand, shows a decrease in energy; this is to be expected as wave breaking occurs and energy is dissipated.

Table 4.1: Comparison between input Hs and calculated Hs

Hs	LINEAR	+-%	SWASH	+-%	OW3D	+-%
0.1	0.1010	+0.95	0.0997	-0.25	0.0948	-5.17
2.0	2.0093	+0.46	1.9938	-0.31	1.8938	-5.31
10.0	10.054	+0.54	9.6204	-3.80	9.1664	-8.34
15.0	15.119	+0.79	13.116	-12.6	17.479	+16.5

Below, the inline Force spectra are shown in Figure 4.5 and Figure 4.6. These show the distribution of the inline force exerted on the structure over the different frequencies. Once again, Figure 4.5 shows the spectrum in a linear sea state. These shapes are in line with the wave spectrum shown in Figure 4.3. Comparing Figure 4.4 to Figure 4.6, what becomes apparent is that the energy at the subharmonics does not lead to increased forces. Meanwhile, the higher harmonics around $f = 0.14Hz$ do show increased peaks when compared to the wave spectrum. Higher frequency waves have shorter wavelengths compared to longer waves; this results in a higher concentration of energy, which in turn leads to increased forces due to steeper slopes and higher amplitudes.

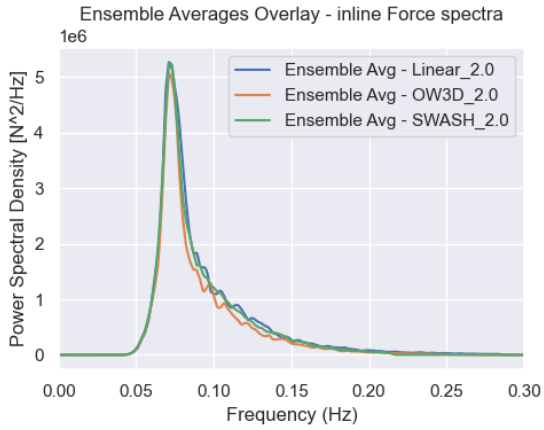

Figure 4.5: Force spectra for $H_s = 2.0$

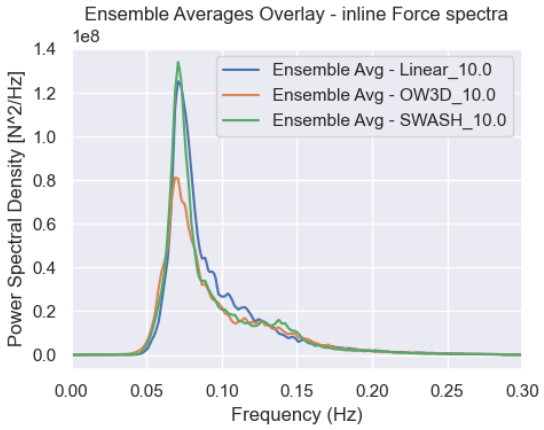

Figure 4.6: Wave spectra for $H_s = 10.0$

Wave Statistics

To analyse the likelihood of events, exceedance probability plots can be used. The upcoming figures, Figure 4.7 and 4.8, show the probability of exceedance for the surface elevation and the wave height. The x-axis denotes the variable of choice, so the surface elevation or the wave height in this case. Where the y-axis shows the probability of the event happening. The y-axis is plotted on a logarithmic scale to emphasize the probabilities at the lower end. The wave height seen in Figure 4.8 has been determined using a zero-crossing analysis. Furthermore, ten realisations of one-hour sea states can be seen for each method. This results in a significant variability in the distributions, especially when looking at the lowest exceedance probabilities. What can also be seen is that the linear theory overestimates the wave height. OW3D and SWASH show the same response, with OW3D being at the lower end of the distribution.

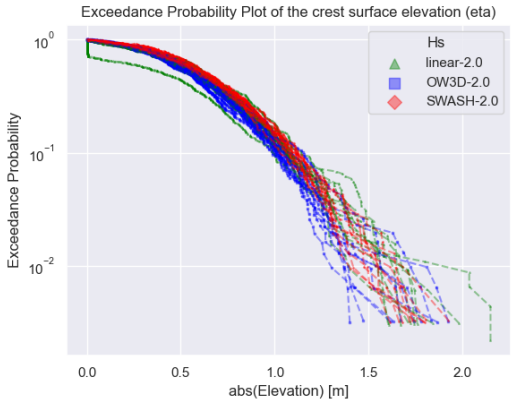

Figure 4.7: Crest surface elevation for $H_s = 2.0$

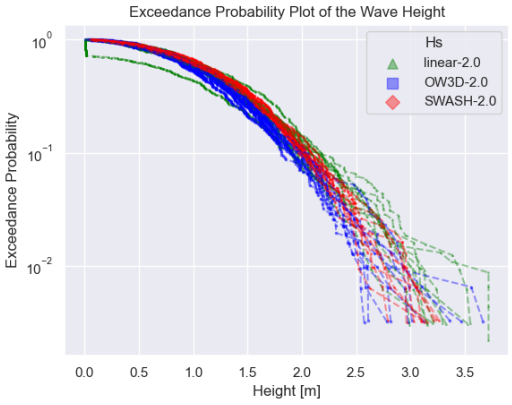

Figure 4.8: Wave height for $H_s = 2.0$

When looking at the non-linear cases seen in Figure 4.9 and 4.10, a clear difference can be seen in the surface elevation. Meanwhile, for the linear case, linear theory underestimates the surface elevation. While being in agreement in terms of wave height. This is where skewness plays a key role; skewness is around 0 for linear waves, as it is through and crest elevations are equal. For non-linear waves, crests will get sharper and troughs flatter. Figure 4.11 and 4.12 show the asymmetry for both axes, with asymmetry over the x-axis being skewness.

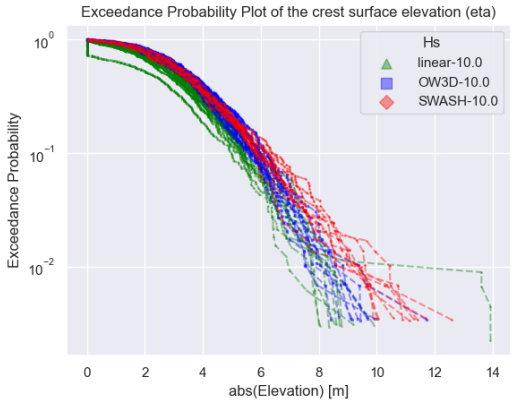

Figure 4.9: Crest surface elevation for $H_s = 10.0$

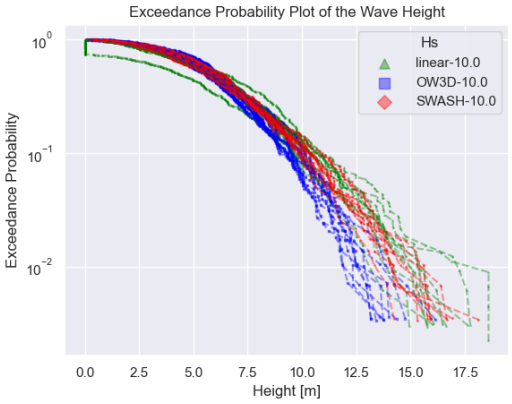

Figure 4.10: Wave height for $H_s = 10.0$

The skewness and asymmetry are calculated over all ten realisations with the formulas mentioned in chapter 2 and are shown in Figure 4.11 and 4.12. The x-axis shows the values, and the y-axis shows which numerical model it is. The legend shows the four different values for H_s. The diamond marker denotes the average value. What can clearly be seen is that the skewness increases as non-linearity increases. Positive skewness indicates sharper crests and flatter troughs. Asymmetry, on the other hand, is less pronounced and only slightly increases when non-linearity is increased. Lastly, the $H_s = 15$ case for OW3D shows questionable results. This adds to the already questionable results seen in the last section.

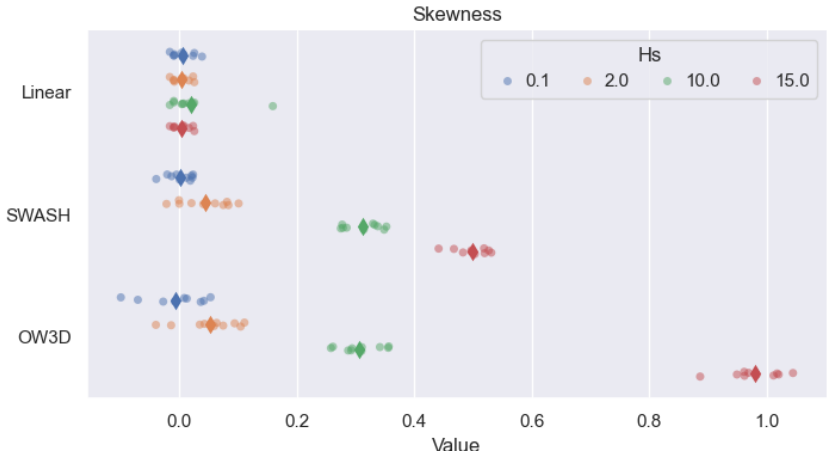

Figure 4.11: Skewness values for all cases, the diamond denotes the average of all 10 cases per program and H_s.

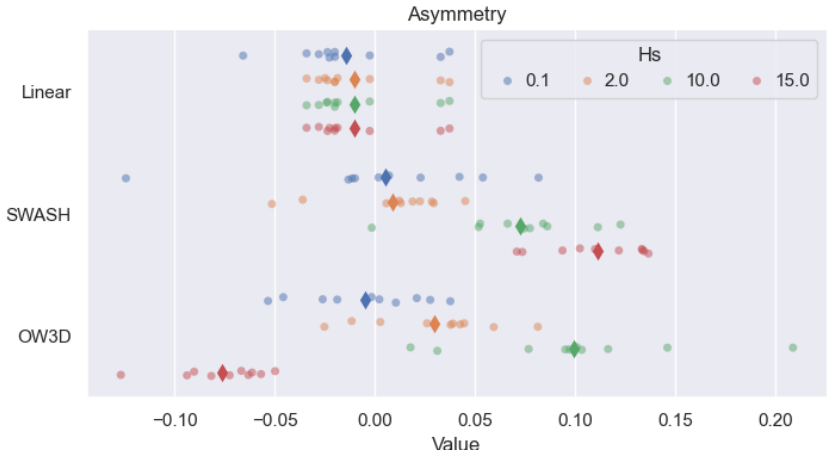

Figure 4.12: Asymmetry values for all cases, the diamond denotes the average of all 10 cases per program and H_s.

How this impacts the forcing can be seen in Figure 4.13 and 4.14. For each wave, the maximum force has been extracted and plotted below. What can be seen is that for the linear case, the total inline force coincides with the wave heights seen in Figure 4.8. But when looking at the non-linear case, the numerical wave tanks report higher forces, which is also in line with the surface elevation reported. With OW3D showing a higher variability and SWASH showing higher forces.

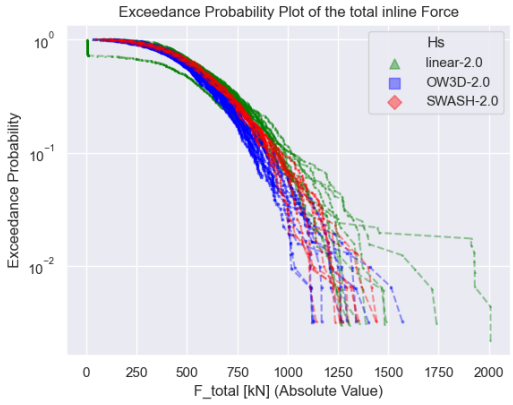

Figure 4.13: Total inline Force for $H_s = 2.0$, linear

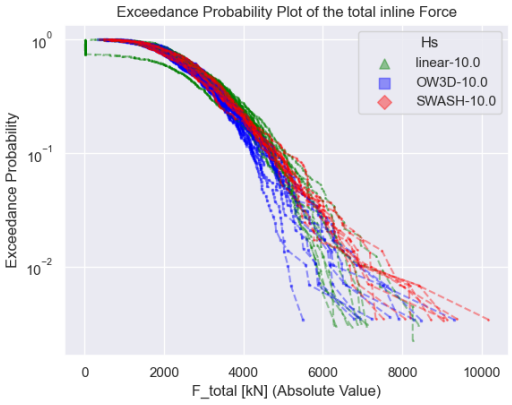

Figure 4.14: Total inline Force for $H_s = 10.0$, non-linear

The biggest differences are seen when looking at the mudline moments. The fully non-linear numerical wave models report much higher moments when looking at the non-linear case. For the linear case, the linear theory seems to overestimate the mudline moment. Once again, SWASH is at the far end in terms of reported moments.

Figure 4.15: Mudline moment for $H_s = 2.0$, linear

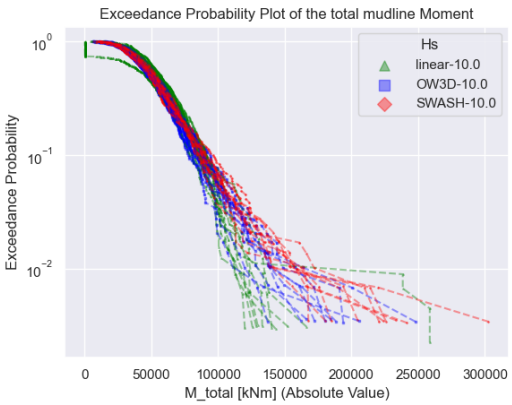

Figure 4.16: Mudline moment for $H_s = 10.0$, non-linear

The case for the most extreme non-linear loads is $H_s = 15.0$. Below, a comparison is shown for the wave shapes and maximum forces for SWASH and OW3D. OW3D shows a steepening wavefront with very high local acceleration. Wave logs for OW3D show that filtering is happening due to the fact that the vertical accelerations exceed the preset limit of $9.81 m/s^2$ at that exact point by a factor of 3. This explains the steepening wavefront rapidly decreasing by OW3D employing filtering. Wave loads reported for OW3D are twice as high as those seen in SWASH.

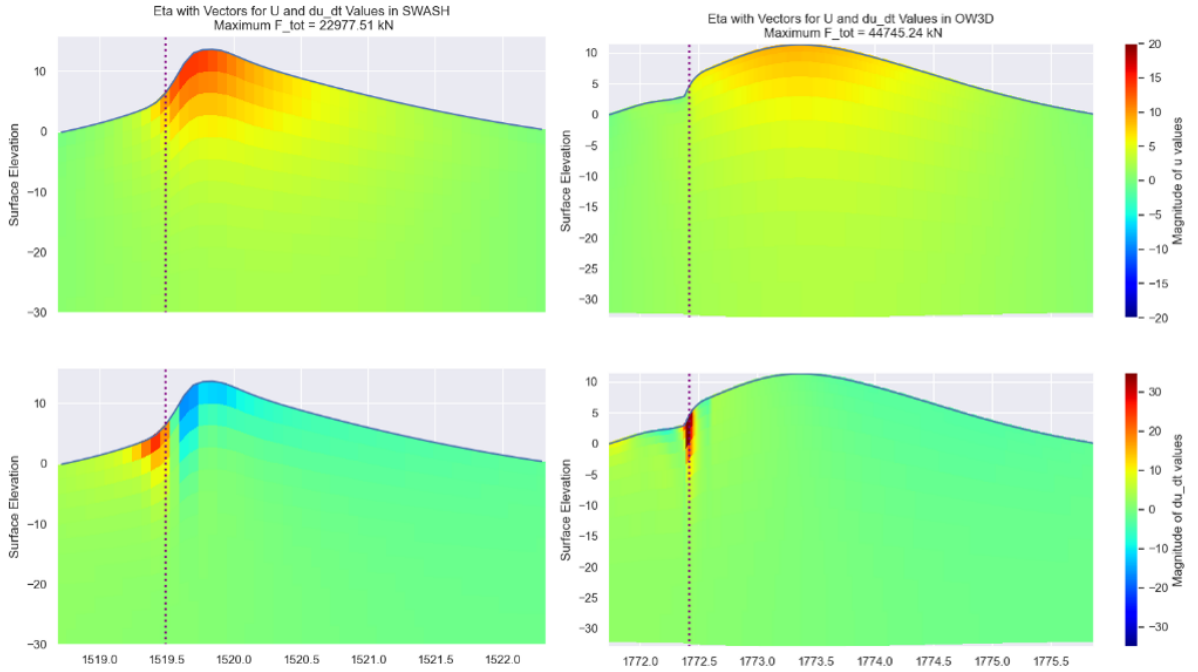

Figure 4.17: Wave height with u and du_dt per layer, for the maximum force seen in the realisations. The dotted line shows the location of maximum force.

4.2.2. Comparison with the Stream Function Method

The maximum forces for all three methods have been plotted in the figure below; since the stream function method should be used for extreme waves and can not go beyond the breaking limit, the case shown is that of $H_s = 10.0$. The stream function method underestimates the forces seen by SWASH and OW3D. The reported maximum forces, orbital velocities and accelerations are reported in Table 4.2. What becomes apparent is that in the non-linear models, the accelerations reported are much higher. Where SWASH reports an increase of 58.1%, which results in an increase of the maximum force of 23.1%. Even while reporting crest heights that are -5.10% less. The velocities are in line for both models. When looking at OW3D, what stands out is that the reported crest height is -18.9% lower while still reporting an increase in maximum- acceleration and force. This again highlights the difference

Table 4.2: Maximum values seen in Figure 4.18 for the stream function method (SF) and the non-linear models SWASH and OW3D. Orbital velocities and accelerations shown are at the crest.

Hs=10.0	SF	SWASH	+-%	OW3D	+-%
max_u [m/s]	7.63	7.76	+1.62	6.83	−10.5
max_du_dt [m/s^2]	4.59	7.25	+58.1	6.49	+41.6
max_force [kN]	$8.27 * 10^3$	$1.02 * 10^4$	+23.1	$9.32 * 10^3$	+9.26
crest height [m]	9.91	9.40	−5.10	8.04	−18.9

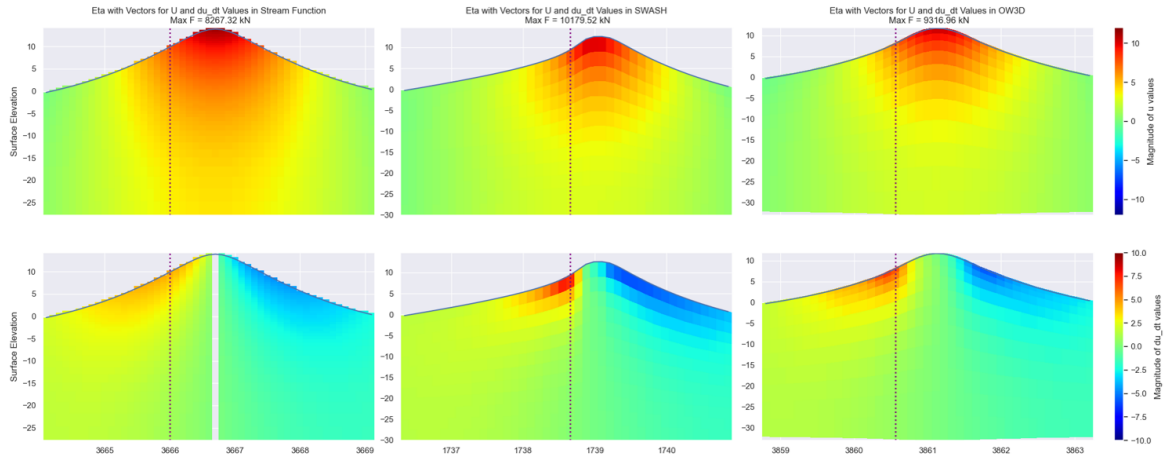

Figure 4.18: Wave height with u and du_dt per layer, for the maximum force seen in the realisations. The dotted line shows the location of maximum force.

5

Discussion

Accurate prediction of loads is a complex and challenging problem which requires careful modelling to ensure high-fidelity output. The fully non-linear waves generated for this research are generated using SWASH and OW3D. A convergence study and a load comparison have been performed to gather insights into how the different wave modelling methods compare with the stream function and one another.

The study is limited to numerical evaluation due to the lack of access to real-world data. While solvers have undergone validation through wave tank experiments, results are still dependent on user setup. In this paper, SWASH shows results that are in line with expectations. Particularly when looking at the total energy captured in the wave spectra, as shown in Table 4.1. When non-linearity increases, total energy decreases, especially in cases where breaking waves are introduced. On the other hand, OW3D shows questionable results, even for the linear simulations. It seems probable that the setup for OW3D is not adequate, as it shows results which are not in line with expectations. Especially for the highly non-linear case where energy is created. This should never be the case, and this leads to the conclusion that the results generated by OW3D can not be trusted. For further research, the convergence study for OW3D should be extended by looking at monochromatic non-linear waves of varying heights. Furthermore, the timestep should also have its own convergence study; as for now, it is reliant on the CFL criterion. The amount of layers chosen in this research is 12, as recommended by the SWASH user manual. This has also been used for OW3D. These values should also be found using a convergence study.

While the results for OW3D can not be trusted, numerical wave models do introduce functionality that can increase the accuracy of modelling non-linear waves and the loads that emerge. For starters, both numerical wave models allow for the creation of custom bathymetries, which allow the user to recreate complex ocean bathymetries and model the interaction. Furthermore, the non-linear models clearly show a distribution of energy to higher harmonics due to triad interactions. These higher harmonics are close to the eigenfrequencies of next-generation wind turbines. A recommendation for further research would thus be to investigate the added fatigue load when looking at fatigue limit state cases.

Furthermore, it is worth noting that SWASH comes with extensive user manuals and setup guides. The input file also offers detailed instructions. Whereas, the input file of the OW3D model offers little to no clarification about input, and the only way to get greater insight is by looking at example files on GitHub. Consequently, the user experience of SWASH is better and less error-prone. It's also worth mentioning that the version of SWASH runs on Windows, while OW3D runs on Linux in VirtualBox. Porting OW3D to Windows would give a fairer benchmark for comparing computational efficiency. Next to both versions being run on different distribution systems, they now also run on a single machine with limited power. This resulted in having to be careful with the duration of the simulations and the amount of waves generated in the experiments. This often meant that, for instance, for the computational efficiency study, single experiments were compared. Whereas running multiple experiments and aver-

aging them would result in a fairer comparison, as background tasks could influence the performance of the models.

The same goes for the load comparison; for this research, ten simulations with different seeds have been run. As can be seen in Figure 4.9, the simulations come with some outliers. To ensure that these outliers do not affect the comparison, all x simulations should be averaged, and the amount of simulations should be increased.

What has been shown is that SWASH reports higher loads than reported by the stream function, by as much as 23%, as shown in Table 4.2. What this implies is that the stream function underestimates the actual load generated. Further research should be done in comparing both models with an experimental wave tank to see if these results are in line with real-world experiments.

Lastly, to calculate the loads, the Morison equation has been used. The Morison equation is valid up to $\pi D/L = 0.20$. When using a JONSWAP spectrum, there will always be waves that go above the limit; these waves should be calculated using diffraction corrections. For instance, the McCamy Fuchs correction. For the most extreme waves analysed in this research, a check has been done to ensure that these fall into the Morison regime.

6

Conclusion

The objective of this research was to see if using the numerical wave models SWASH and OW3D as numerical wave tanks would offer better insights into analysing the impact of non-linear waves on next-generation wind turbines. This main question was divided into three parts, with the first being a comparison between linear theory, SWASH and OW3D in both linear and non-linear sea states. During the convergence study in Chapter 3, OW3D showed promising results by reporting lower errors and higher computational efficiency. But when comparing both models to linear theory, OW3D showed large errors, even for the linear cases ($H_s = [0.1, 2.0]$). Furthermore, when looking at the most extreme case ($H_s = 15.0$), OW3D even reported an increase in energy throughout the simulation. Next, it shows filtering and very large concentrated accelerations in chapter 4. This has led to the conclusion that the results for OW3D in this paper can not be trusted; this is probably due to the fact that OW3D is improperly set up. SWASH, on the other hand, did show promising results in both sea states. It showed small errors in terms of Hs in both linear sea states and increasing errors when non-linearity was increased. What became evident from the simulations against the linear theory is that the non-linear models have increased skewness, which results in increased surface elevation compared to the linear model. This, in turn, leads to higher forces and overturning moments.

The second research question is about tuning the parameterized breaking criterion of OW3D. To ensure it aligns with the breaking response seen in SWASH, where SWASH solves breaking numerically with hydraulic bores. In chapter 2, two papers have been referenced, which both investigated the breaking criterion for non-linear potential flow solvers like OW3D. These papers both came to the same conclusion that for accurate detection of breaking wave initiation, the user-defined parameter should be set to 1. Therefore, no further investigation has been done to have OW3D have the same breaking response as SWASH; instead, the parameter has been set to 1 to ensure the breaking wave detection is as accurate as possible for OW3D.

The third question looked at comparing the loads calculated with SWASH and OW3D to the stream function method. subsection 4.1.1 looked into comparing these three models. What is to be concluded is that during the 10 one-hour sea states simulated in SWASH, for the case of $H_s = 10.0$, a $+23.1$% increase in maximum force is reported with respect to the stream function method. With a crest height which is -5.10% lower for SWASH. Both the crest- velocities and acceleration are higher for SWASH, with especially the crest accelerations being 58.1% higher. This leads to the conclusion that the non-linear model SWASH report much higher accelerations, which increases the maximum load exerted on the structure. The results for OW3D also report loads that are 9.26% higher but can not be trusted.

In conclusion, this study highlights the significance of considering non-linear wave effects when calculating loads on structures in non-linear sea states. This study has shown the stream function method to underestimate the loads on a structure in non-linear sea states and that numerical wave models can be used to provide load calculations on next-generation wind turbines.

References

Amano, R. S. (2017). Review of Wind Turbine Research in 21st Century. https://doi.org/10.1115/1.4037757

Bracewell, R. N. (2000). *The Fourier Transform And Its Applications - Bracewell*.

Bredmose, H., Dixen, M., Ghadirian, A., Larsen, T. J., Schløer, S., Andersen, S. J., Wang, S., Bingham, H. B., Lindberg, O., Christensen, E. D., Vested, M. H., Carstensen, S., Engsig-Karup, A. P., Petersen, O. S., Hansen, H. F., Mariegaard, J. S., Taylor, P. H., Adcock, T. A., Obhrai, C., … Hanson, T. D. (2016). DeRisk - Accurate Prediction of ULS Wave Loads. Outlook and First Results. *Energy Procedia*, *94*, 379–387. https://doi.org/10.1016/j.egypro.2016.09.197

Chakrabarti, S. (1987). Hydrodynamics of offshore structures. https://books.google.com/books?hl=nl&lr=&id=RNGW9CucxQsC&oi=fnd&pg=PP1&ots=spG5Jvod_W&sig=8riPKhoLUHIPFE4t1x1OI_HU0UM

Dean, R. G. (1965). *Stream Function Representation of Nonlinear Ocean Waves* (tech. rep. No. 18).

Düz, B., Bunnik, T., & Kapsenberg, G. (2016). NUMERICAL SIMULATION OF NONLINEAR FREE SURFACE WATER WAVES USING A COUPLED POTENTIAL FLOW-URANS/VOF APPROACH. http://swash.sourceforge.net,

Engsig-Karup, A. P., Bingham, H. B., & Lindberg, O. (2009). An efficient flexible-order model for 3D nonlinear water waves. *Journal of Computational Physics*, *228*(6), 2100–2118. https://doi.org/10.1016/J.JCP.2008.11.028

Engsig-Karup, A. P., Madsen, M. G., & Glimberg, S. L. (2012). A massively parallel GPU-accelerated model for analysis of fully nonlinear free surface waves. *International Journal for Numerical Methods in Fluids*, *70*(1), 20–36. https://doi.org/10.1002/fld.2675

Everen De Vries, W., & Vorpahl, F. (n.d.). *Final report WP 4.2: Support Structure Concepts for Deep Water Sites: Deliverable D4.2.8 (WP4: offshore foundations and support structures)* (tech. rep.). https://www.researchgate.net/publication/241886865

Fenton, J. D. (1988). *THE NUMERICAL SOLUTION OF STEADY WATER WAVE PROBLEMS* (tech. rep. No. 3).

IEC. (2019). *IEC 61400-3-1 Design requirements for fixed offshore wind turbines* (1.0).

Le Mehaute, B. (1976). An introduction to hydrodynamics and water waves. https://doi.org/10.1007/978-3-642-85567-2/COVER

MacCamy & Fuchs. (1954). *WAVE FORCES ON PILES: A DIFFRACTION THEORY* (tech. rep.).

Manners W. & Rainey R.C.T. (1992). *Hydrodynamic forces on fixed submerged cylinders* (tech. rep.). University of Leicester. https://royalsocietypublishing.org/

Morison, J. R., O'brien, M. P., Johnson, J. W., & Schaaf, S. A. (1950). *THE FORCE EXERTED BY SURF'ACE W AVES ON PILES THE FORCE EXERTED BY SURF ACE WAVES ON PILES* (tech. rep.). http://onepetro.org/JPT/article-pdf/2/05/149/2238818/spe-950149-g.pdf/1

Paulsen, B. T., Bredmose, H., & Bingham, H. B. (2014). An efficient domain decomposition strategy for wave loads on surface piercing circular cylinders. *Coastal Engineering*, *86*, 57–76. https://doi.org/10.1016/j.coastaleng.2014.01.006

Paulsen, B. T., Bredmose, H., Bingham, H. B., & Schløer, S. (2013). Steep wave loads from irregular waves on an offshore wind turbine foundation: Computation and experiment. *Proceedings of the International Conference on Offshore Mechanics and Arctic Engineering - OMAE*, *9*. https://doi.org/10.1115/OMAE2013-10727

Pavilons, D., Hengelmolen, V., Plenker, D., Bruinsma, N., Biermans, L., Smale, A., & Wellens, P. (2022). *Hydrodynamic loading of breaking waves of breaking waves on offshore inspection platforms* (tech. rep.).

Peeringa, J. M. (2004). *Wave loads on offshore wind turbines Feasibility study using results of wave experiments executed by Electricité de France (EDF)* (tech. rep.).

Roo, D. E., Suzuki, T., Kolokythas, G., Zhao, G., & Verwaest, T. (2015). *NUMERICAL MODELLING OF 2D WAVE TRANSFORMATION PROCESSES FROM NEARSHORE TO A SHALLOW FORE-*

SHORE: COMPARISON BETWEEN THE MIKE21, SWASH AND XBEACH MODELS (tech. rep.).

Schløer, S., Bredmose, H., & Bingham, H. B. (2016). The influence of fully nonlinear wave forces on aero-hydro-elastic calculations of monopile wind turbines. *Marine Structures*, *50*, 162–188. https://doi.org/10.1016/j.marstruc.2016.06.004

Smit, P., Zijlema, M., & Stelling, G. (2013). Depth-induced wave breaking in a non-hydrostatic, near-shore wave model. *Coastal Engineering*, *76*, 1–16. https://doi.org/10.1016/j.coastaleng.2013.01.008

Stelling, G. S., & Zijlema, M. (2009). *Numerical modeling of wave propagation, breaking and run-up on a beach* (tech. rep.).

Suja-Thauvin, L., Krokstad, J. R., & Bachynski, E. E. (2018). Critical assessment of non-linear hydrodynamic load models for a fully flexible monopile offshore wind turbine. *Ocean Engineering*, *164*, 87–104. https://doi.org/10.1016/j.oceaneng.2018.06.027

Tang, Y., Shi, W., Ning, D., You, J., & Michailides, C. (2020). Effects of Spilling and Plunging Type Breaking Waves Acting on Large Monopile Offshore Wind Turbines. *Frontiers in Marine Science*, *7*. https://doi.org/10.3389/fmars.2020.00427

Varing, A., Filipot, J.-F., Grilli, S., Duarte, R., Roeber, V., & Yates, M. (n.d.). *A new definition of the kinematic breaking onset criterion validated with solitary and quasi-regular waves in shallow water* (tech. rep.).

Vázquez, A., Izquierdo, U., Enevoldsen, P., Andersen, F. H., & Blanco, J. M. (2022). A macroscale optimal substructure selection for Europe's offshore wind farms. *Sustainable Energy Technologies and Assessments*, *53*, 102768. https://doi.org/10.1016/J.SETA.2022.102768

Velarde, J., Vanem, E., Kramhøft, C., & Sørensen, J. D. (2019). Probabilistic analysis of offshore wind turbines under extreme resonant response: Application of environmental contour method. *Applied Ocean Research*, *93*. https://doi.org/10.1016/j.apor.2019.101947

Vyzikas, T., Stagonas, D., Maisondieu, C., & Greaves, D. (2021). Intercomparison of three open-source numerical flumes for the surface dynamics of steep focused wave groups. *Fluids*, *6*(1). https://doi.org/10.3390/fluids6010009

Wang, S., Larsen, T. J., & Bredmose, H. (2021). Ultimate load analysis of a 10 MW offshore monopile wind turbine incorporating fully nonlinear irregular wave kinematics. *Marine Structures*, *76*. https://doi.org/10.1016/j.marstruc.2020.102922

Zijlema, M. (2010). swash user manual.

Zijlema, M. (2019). The role of the Rankine-Hugoniot relations in staggered finite difference schemes for the shallow water equations. *Computers and Fluids*, *192*. https://doi.org/10.1016/j.compfluid.2019.104274

Zijlema, M., Stelling, G., & Smit, P. (2011a). Simulating nearshore wave transformation with non-hydrostatic wave-flow modelling. http://swash.sourceforge.net

Zijlema, M., Stelling, G., & Smit, P. (2011b). SWASH: An operational public domain code for simulating wave fields and rapidly varied flows in coastal waters. *Coastal Engineering*, *58*(10), 992–1012. https://doi.org/10.1016/j.coastaleng.2011.05.015

A

Appendix

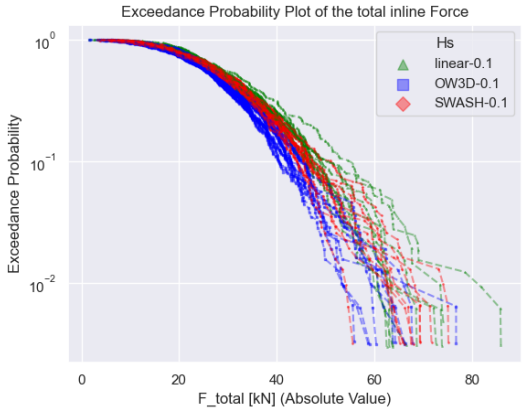

(a) Inline force for $H_s = 0.1$

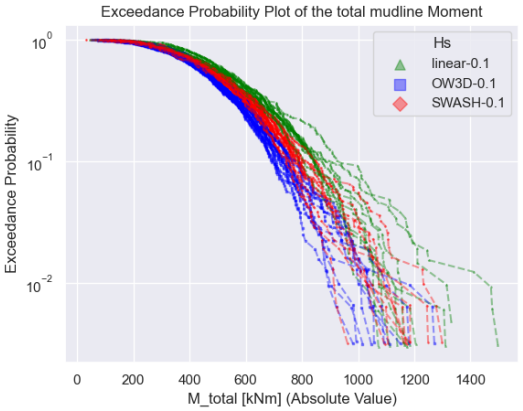

(b) Mudline moment for $H_s = 0.1$

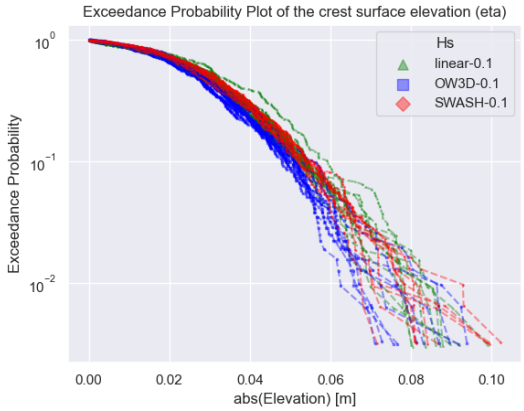

(c) Surface elevation for $H_s = 0.1$

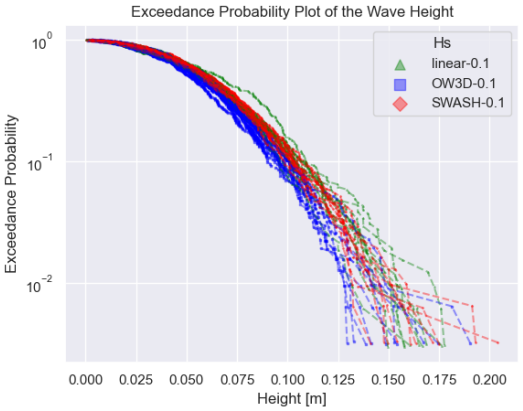

(d) Wave height for $H_s = 0.1$

Figure A.1: The exceedance plots for the case of $H_s = 0.1$

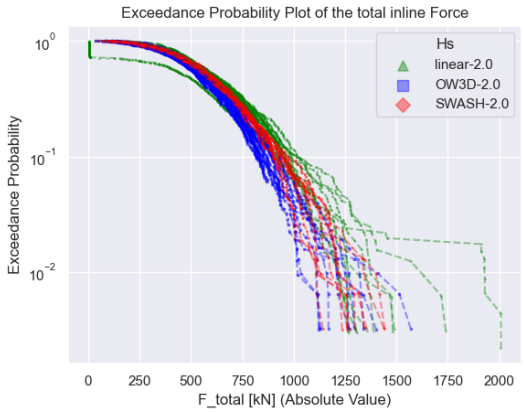

(a) Inline force for $H_s = 2.0$

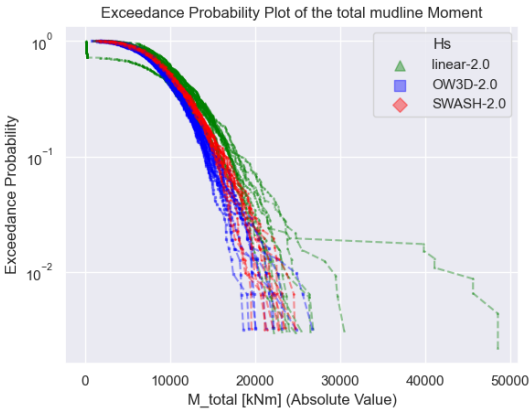

(b) Mudline moment for $H_s = 2.0$

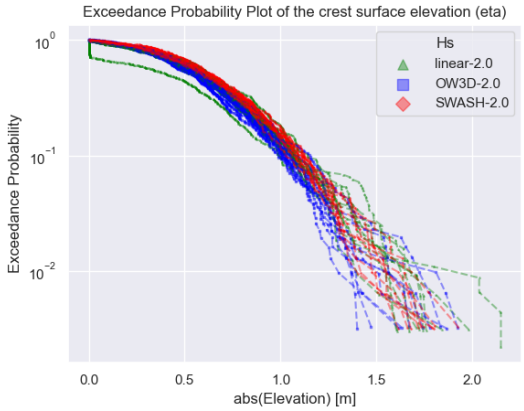

(c) Surface elevation for $H_s = 2.0$

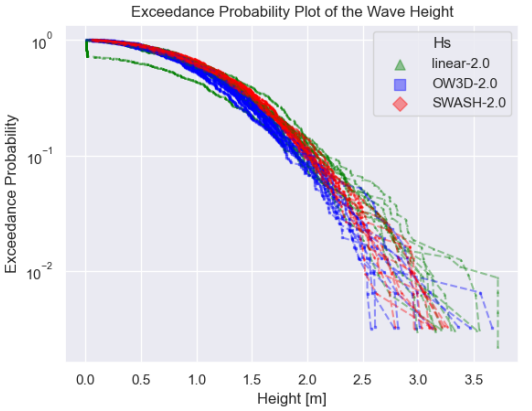

(d) Wave height for $H_s = 2.0$

Figure A.2: The exceedance plots for the case of $H_s = 2.0$

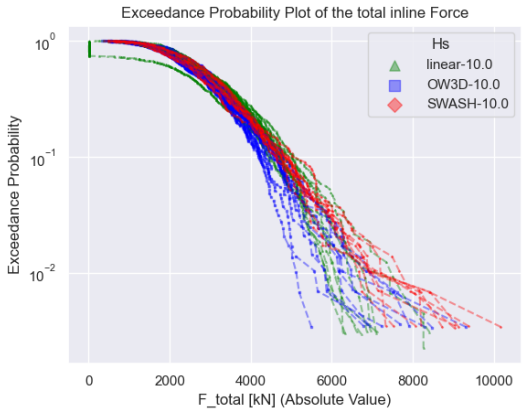

(a) Inline force for $H_s = 10.0$

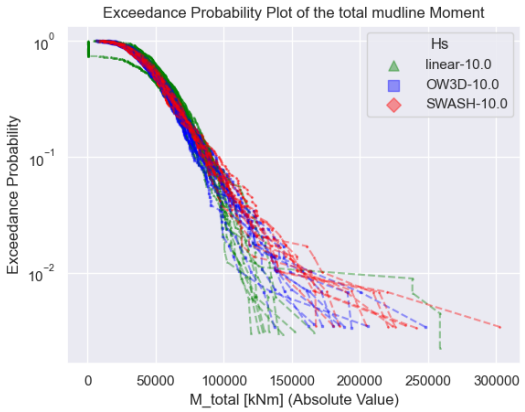

(b) Mudline moment for $H_s = 10.0$

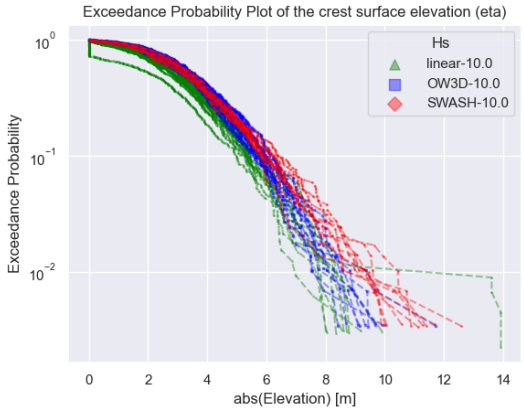

(c) Surface elevation for $H_s = 10.0$

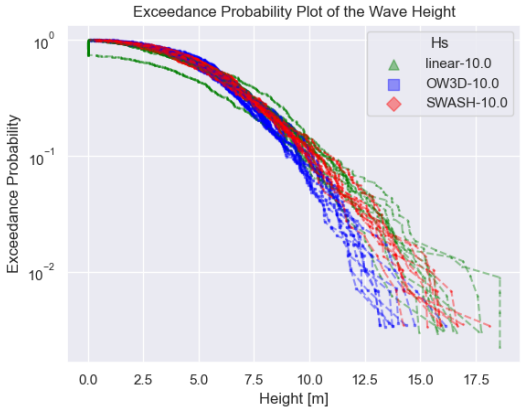

(d) Wave height for $H_s = 10.0$

Figure A.3: The exceedance plots for the case of $H_s = 10.0$

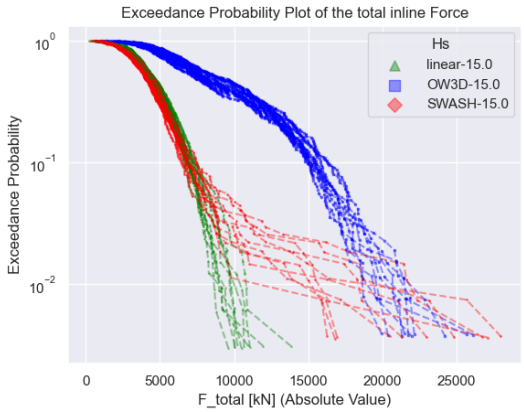

(a) Inline force for $H_s = 15.0$

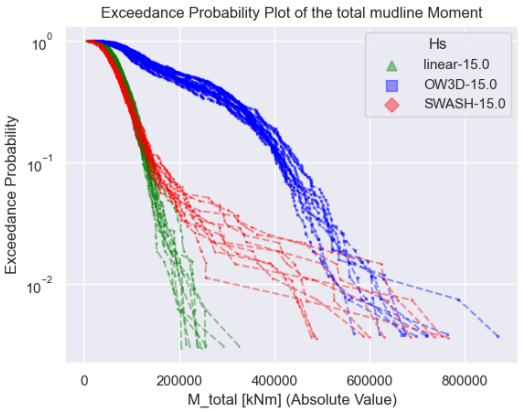

(b) Mudline moment for $H_s = 15.0$

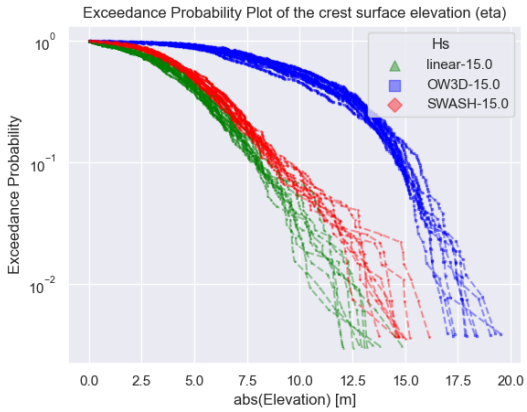

(c) Surface elevation for $H_s = 15.0$

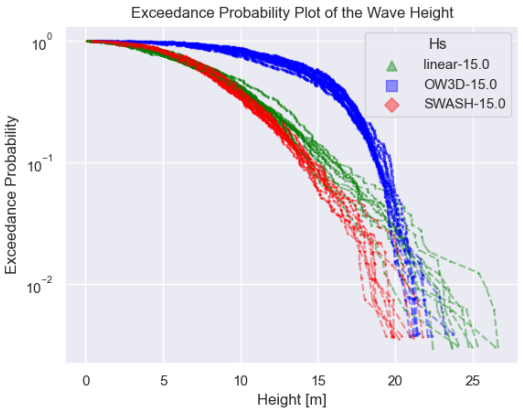

(d) Wave height for $H_s = 15.0$

Figure A.4: The exceedance plots for the case of $H_s = 15.0$

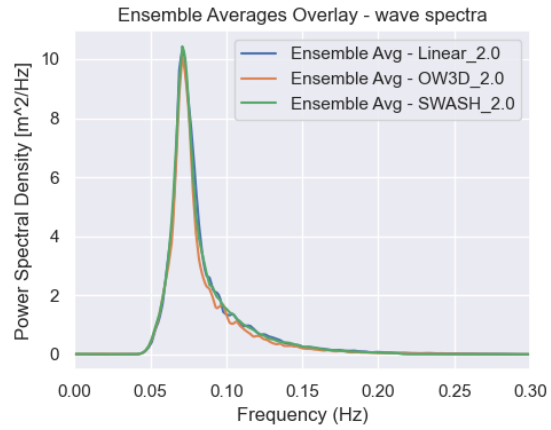

Figure A.5: Wave spectra for $H_s = 2.0$, SWASH, OW3D and linear theory.

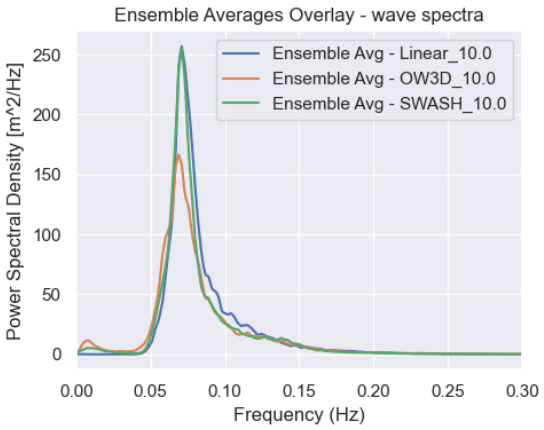

Figure A.6: Wave spectra for $H_s = 10.0$, SWASH, OW3D and linear theory.

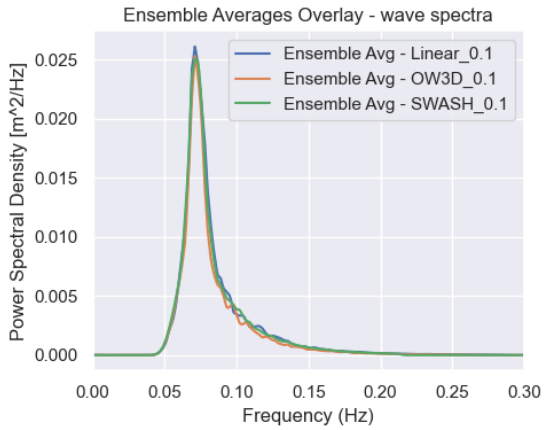

Figure A.7: Wave spectra for $H_s = 0.1$, SWASH, OW3D and linear theory.

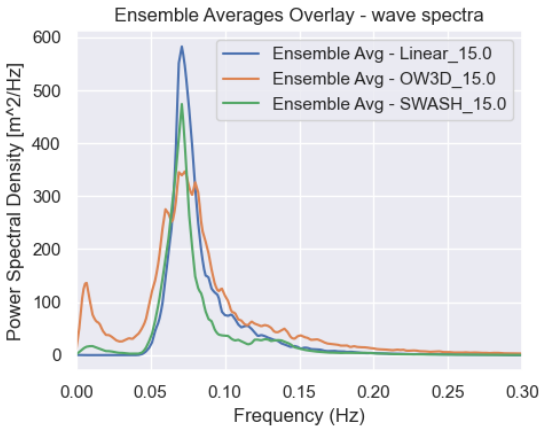

Figure A.8: Wave spectra for $H_s = 15.0$, SWASH, OW3D and linear theory.

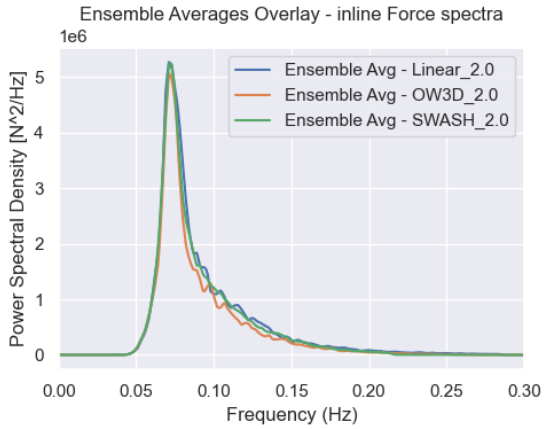

Figure A.9: Force spectra for $H_s = 2.0$, SWASH, OW3D and linear theory.

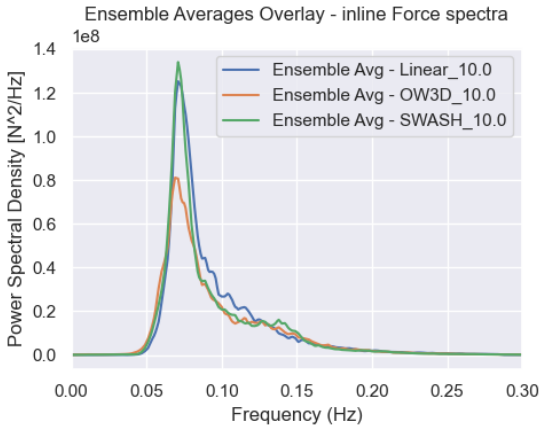

Figure A.10: Wave spectra for $H_s = 10.0$, SWASH, OW3D and linear theory.

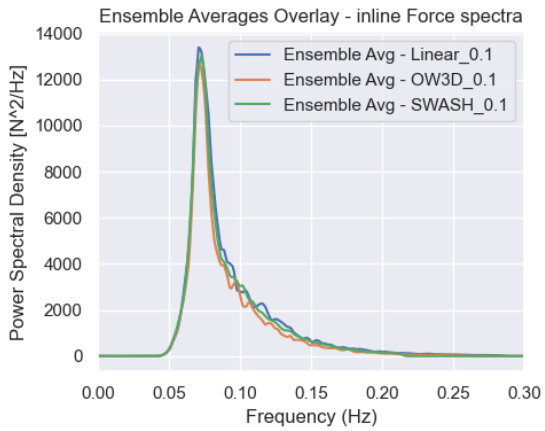

Figure A.11: Force spectra for $H_s = 0.1$, SWASH, OW3D and linear theory.

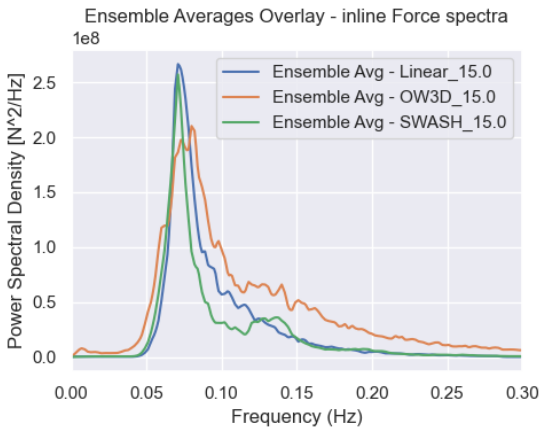

Figure A.12: Wave spectra for $H_s = 15.0$, SWASH, OW3D and linear theory.